TECHNISCHE
UNIVERSITÄT
WIEN
Vienna | Austria

DIPLOMA THESIS

Perturbed angular correlation and x-ray diffraction studies on the alpha-beta phase transition in multiferroic bismuth ferrite

submitted in satisfaction of the requirements for the degree of Diplom-Ingenieur of the
TU Wien, Faculty of Technical Chemistry

carried out at the X-Ray Center
of the Vienna University of Technology

in collaboration with

the ISOLDE Solid State Physics Group, ISOLDE at CERN, Geneva,
Switzerland

under the supervision of

Dr.techn. Berthold Stöger
and
Dr. Juliana Schell

through

Georg Marschick BSc.

MatNr. 1129923

May 25, 2020

Declaration of Authorship

I hereby declare that the thesis submitted is my own unaided work. All direct or indirect sources used are acknowledged as references. The measurements used to create this work were carried out at the Isotope separator on-line device, ISOLDE, at CERN in Geneva, Switzerland and at the X-ray center of the Vienna University of Technology in Vienna, Austria. The data analysis was done by myself under the guidance of my supervisors Dr.techn. Berthold Stöger and Dr. Juliana Schell. Parts of this work are in process of being published in the paper *Multiferroic Bismuth Ferrite: First PAC and XRD studies on its ferroic* α *-* β *phase transition - Georg Marschick et al.* at Physical Review B.

Vienna, May 25, 2020

Abstract

Multiferroic materials draw attention owing to the exhibition of more than one ferroic form (ferroelectricity, ferromagnetism or ferroelasticity) in the same phase. The main focus of this work lies on materials combining ferroelectricity with ferromagnetism as this combination theoretically allows direct electrically controlled magnetism and magnetically controlled electric polarisation. The advantages of such combinations are obvious by opening a whole new degree of freedom in material and device design, potentially expanding possibilities in storage management and computing power.

One problem with most multiferroics is the fact that the magnetic Neél temperature and the electric Curie temperature often are low, usually below room temperature, leading to a loss of multiferroic behaviour in technically desired temperature ranges. However, Bismuth ferrite, also referred to as $BiFeO_3$ or simply BFO, is one promising candidate for industrial applications as its Neél and Curie temperature points are well above room temperature. Bismuth ferrite appears in three different phases, the α-phase at room temperature and two high temperature phases namely the β-phase and the γ-phase before decomposing and melting, with all off them showing different crystal structures. As the outcome of numerous research groups showed different results regarding the β-phase, the nature of the β-phase and the α-β phase transition were supervised in this work.

Perturbed Angular Correlation (PAC) measurements done at the ISOLDE Solid State Physics Group at ISOLDE, CERN in Geneva, Switzerland were combined with X-Ray diffraction (XRD) measurements done at the X-Ray center of the Vienna University of Technology in Vienna, Austria. The results confirm a proposed $Pbnm$ crystal symmetry of the β-phase with a phase transition temperature of $T_{\alpha-\beta} = 820°C$. The combination of the two measurement methods and especially the usage of ^{111m}Cd as the PAC probe to characterize BFO was performed the first time by our group.

Zusammenfassung

Multiferroische Materialien ziehen durch das Veräußern von mehr als einem ferroischen Ordnungsparameter in der selben Phase Aufmerksamkeit auf sich. Materialien welche Ferroelektrizität und Ferromagnetismus kombinieren, stehen besonders im Fokus, da diese Kombination eine direkt durch Elektrizität kontrollierte Magnetisierung bzw. eine direkt durch ein Magnetfeld hervorgerufene elektrische Polarisierung eines Materials bewirken kann. Die Vorteile solcher Materialien sind offensichtlich und öffnen einen neuen Freiheitsgrad bei der Material-, und Bauteilentwicklung mit Anwendungen in der Speicher-, und Computertechnologie.

Ein Hauptproblem von multiferroischen Materialien sind die Einsatztemperaturen. Da die magnetische Neél Temperatur und die elektrische Curie Temperatur oft weit unter Raumtemperatur liegen, verlieren die meisten Multiferroika ihre Eigenschaften bei Raumtemperatur, was die technischen Anwendungsbereiche weit einschränkt. Bismuthferrit, $BiFeO_3$ oder kurz einfach BFO genannt, jedoch ist ein vielversprechender Kandidat für Anwendungen im Raumtemperaturbereich, da die Neél Temperatur und die Curie Temperatur weit darüber liegen. Bismuthferrit tritt in drei verschiedenen Phasen auf, der rhomboedrischen α-Phase bei Raumtemperatur und zwei Hochtemperaturphasen, der β-Phase und der γ-Phase kurz vor dem Schmelzpunkt. Unterschiedliche Ergebnisse bezüglich der Struktur der β-Phase und der α-β Phasenübergangstemperatur führten zu einer weiteren Untersuchung dieses Phasenüberganges in dieser Arbeit. Mittels Messungen mit gestörter Winkelkorrelation (Perturbed Angular Correlation, PAC), welche mit der ISOLDE Solid States Physics Group bei ISOLDE, CERN in Genf, Schweiz durchgeführt wurden, kombiniert mit Röngtendiffraktometrieuntersuchungen (X-ray diffraction, XRD), durchgeführt am Röntgeninstitut der Technischen Universität Wien, konnten die Kristallstruktur als orthorhombisch $Pbnm$ und die Phasenübergangstemperatur bei $T_{\alpha-\beta} = 820°C$ bestätigt werden. Die Kombination der beiden Messmethoden und generell die PAC Messungen mit ^{111m}Cd, einem Cadmiumisomer, als Sonde, wurden von uns zum ersten Mal zur Charakterisierung von BFO verwendet.

Acknowledgements

The success of any project, especially of research projects, is usually a combination of many hands and minds. In respect thereof i would like to take this opportunity to acknowledge some persons which directly and indirectly influenced the process and success of this work.

First of all I would like to thank my main supervisor *Dr. Berthold Stöger* from the X-Ray center of the Vienna University of Technology and *Dr. Juliana Schell*, my supervisor at the Solid State Physics Group at ISOLDE, CERN, for their mentorship and guidance throughout the whole process of formation of this work and beyond that. I deeply appreciate their efforts and time taken to read through drafted documents, reports and the thesis, always putting a critical eye on it. Their comments, suggestions and consultations always guided me into the right way.
Special thanks also to *João N. Gonçalves* from the Universidade de Aveiro, Portugal, for your DFT calculations and your continuous support during this project.

I am deeply grateful to all collaborators of the X-Ray Center of the Vienna University of Technology, especially to *DI. Werner Arnter* for technical and theoretical assistance in all thinkable aspects and the infinite patience needed to conduct my measurements, as well as to *Dr. Klaudia Hradil* for the coordination and acceptance of this work. Further i am greatly indebted to all colleagues of the Solid State Physics Group at ISOLDE, CERN. Special thanks go out to *Dr. Karl Johnston* for coordinating the beam times and having me welcome everytime as well as to *Dr. João Guilherme Martins Correia* for excellent technical and theoretical assistance and help during the beamtimes and the PAC measurements. The same holds true for *Mr. Dmitry Zyabkin*, thank you for your input and help during hours of skype communications.

Last but not least my deepest appreciations go to my family and my friends, especially to *C. Mane* and *H. Bomba*, for never letting off me also during difficult phases with days and nights spent studying at university. Without you this would not be possible.

Contents

1 Introduction and Background

1.1 Primary Ferroic Forms

A primary ferroic material is characterized by the exhibition of either spontaneous magnetisation, electric polarisation or a spontaneous strain while being in an equilibrium condition meaning that no external fields or forces are acting on it. These orders can be switched or reversed through the application of sufficiently high extrinsic fields, magnetic fields for reversing the magnetisation in ferromagnets, electric fields to switch polarisation in ferroelectrica and stress to change strain in ferroelastic materials. As opposed to what the name suggests, ferroic forms are not linked to the existence of iron (lat. ferrum) but were named referring to the hysteresis occurring when switching the magnetisation through the appliance of an external magnetic field in ferromagnetic materials. Hysteresis effects also occur in ferroelectric and ferroelastic materials.[1]

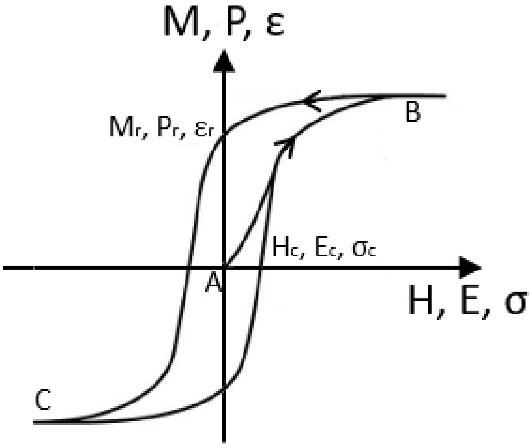

Figure 1.1: Schematic of a hysteresis showing coercive field strengths H_c and E_c, coercive stress σ_c as well as remanent magnetisation M_r, polarisation P_r and strain ϵ_r.

1.1.1 Ferroelectricity

Ferroelectricity was originally observed in Rochelle Salt ($KNaC_4H_4O_6.4H_2O$) by J. Valasek[2] in 1920. Ferroelectric materials behave different than other dielectric materials when exposed to an electric field. Unlike pyroelectric crystals which show a permanent electric polarisation fixed in one direction, ferroelectric materials have the property of switching the polarisation direction. The relation between electric field strength and polarisation follows a hysteresis curve shown in Figure 1.1. Prior to the application of an external field (point A in Figure 1.1), the material shows no net polarisation as the domains are randomly arranged. Domains are regions in the crystal where the polarisation direction is uniform. As the electric field E grows, domains which point in the field direction will grow, eventually leading to saturation when all domains are aligned with the external field. This saturation point is marked as point B in figure 1.1. If the field is switched off now, the remanent polarisation of the crystal P_r will remain. To change the polarisation direction, the external field has to be applied in opposite direction with sufficient field strength. The curve in figure 1.1 follows the path between point B and C crossing the zero polarisation line when the coercive field strength is applied, eventually reaching opposite saturation at point C.[3]

The reason some materials are able to show spontaneous polarisation and others are not can be found at the atomic level and is achieved by an off-centering of cations and anions, moving the centers of charges, eventually leading to a bulk polarisation. Most technologically important ferroelectrics are transition metal oxides, where the transition metal ions possess empty d-electron shells. There, the polarisation usually is caused by the movement of positively charged ions with respect to their oxygen coordination polyhedron.[4] Though, there are numerous other groups of ferroelectric materials, which do not belong to the group of transition metal oxides. According to the crystallographic restriction theorem, crystals can adopt one of the 32 crystallographic point groups, which correspond to the 32 crystal classes. These can be classified into two families: 11 with and 21 without inversion symmetry. Crystals of the latter are non-centrosymmetric. Centrosymmetric crystals are per se not able to be polarized as for every existing permanent dipole moment a counterpart in the opposite direction exists which cancels out a polarisation. Crystals crystallizing in 20 of the 21 non-centrosymmetric point groups are piezoelectric meaning that they show at least one polar axis and thus allow polarisation through mechanical stress. The only exception are crystals with the 432 point group as they are non-centrosymmetric and also show non polarity.[5] Ten of these 20 crystal classes only show one polar axis making crystals pyroelectrics, showing spontaneous polarisation when heated up. Some of them were proven to be ferroelectrics, able to change the direction of polarisation.[6] One example of a structure family whose members often show ferroelectric behaviour are perovskites. BFO belongs to this structure family.

1.1.2 Ferromagnetism

The phenomenon of ferromagnetism has been known for centuries, long before electromagnetism was discovered. Magnetite as a natural magnet was for example used for the manufacturing of compass needles, essential for navigating and exploring new worlds. The physical background though, for a long time was not understood.

A ferromagnetic material, in analogy to a ferroelectric material, shows a permanent magnetisation below a certain temperature T_c, the Curie Temperature. Again, this magnetisation does not necessarily appear as a macroscopic net magnetisation as in a permanent magnet. This is due to magnetic domains, areas with uniform magnetisation direction, which are oriented randomly in the macroscopic crystal when no external magnetic field is applied. When the material is magnetised, the relation between the magnetic field strength H and the material's magnetisation M again follows the hysteresis curve shown in figure 1.1. Starting at zero field and zero magnetisation at point A, saturation is reached at point B when the field is sufficiently strong. Switching off the magnetic field leaves the magnetic material with the remanent magnetisation M_r. To demagnetize the material, the coercive field strength H_c has to be applied in the opposite direction. The ferromagnetic material can be magnetised in the opposite direction by increasing the field strength until saturation is reached again (point C in figure 1.1).

The physical background of course is a very different one compared to ferroelectricity and also is also somewhat more complex. While in ferroelectric materials, as explained in section 1.1.1 the shifting of charge distribution centres, which can be assigned to the movement of atoms, causes the effect, the phenomenon of ferromagnetism is caused by unpaired electrons and their spins. Thus, in magnetism partly filled electron shells are required in order to build up a net magnetic spin moment.[4] As the magnetic dipole-dipole interaction is too weak to cause a long-range spontaneous alignment of magnetisation the material, other mechanisms must be responsible for the formation of magnetic interaction. These quantum mechanic mechanisms are the so called exchange interaction as well as the RKKY (Ruderman–Kittel–Kasuya–Yosida) interaction.[7]

1.1.3 Ferroelasticity

The phenomenon of ferroelasticity is more difficult to visualise compared to the other two primary ferroic forms. As ferroelasticity is not linked to the research in this work, the phenomenon is described here only briefly.
In ferroelastic materials, the stress strain curve does not follow a classic linear (elastic regime) / nonlinear (plastic regime) behaviour like it does in a conventional material. However, as is the case in the other promary ferroic forms, it follows a hysteresis like the one shown in Figure 1.1. By applying an external stress, the orientation of the crystal can be switched between at least two different orientations.[8]

1.2 Multiferroic Forms

As opposed to the primary ferroic forms, multiferroic phenomena exhibit more than one primary ferroic form in the same phase. Interactions between these primary ferroic forms do not necessarily have to occur, though many ferroelectric materials also show ferroelasticity, leading to the piezoelectric effect. Most ferroelectric perovskites are transition metal oxides. The origin of their ferroelectricity is usually the formation of molecule clusters through the positively charged transition ions with an empty d^0 electron shell and negative oxygen ions of their nearest surrounding. The shift of the anions and cations leads to a net electric polarisation of the crystal.[4, 9]

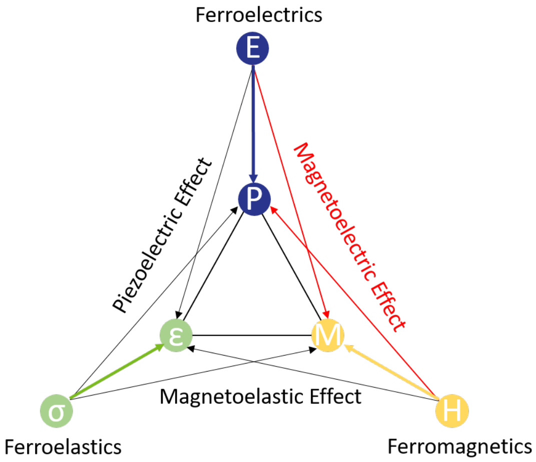

Figure 1.2: The triangle shows all three primary ferroic forms and their connections through multiferroic effects. The magnetoelectric effect is highlighted in red

Unfortunately, only few materials show the high potential combination of ferroelectricity and ferromagnetism. This is the result of the origins of both these phenomena, which are mutually exclusive.[10] While ferroelectricity is often exhibited by materials with transition metal ions with empty d-electron shells as explained above, ferromagnetism can only develop with semi filled d-electron shells in order to achieve a net spin value crucial for a magnetic moment.[4] Figure 1.2 shows the connection between the three primary ferroic forms and their order parameters. As mentioned, the combination between ferroelasticity and electrical polarizability leads to the (inverse) piezoelectric effect while combined with a ferromagnetic ordering the (inverse) magnetoelastic (magnetostriction) effect are achieved.

1.2.1 Magnetoelectric (ME) Multiferroics

The magnetoelectric effect, combining ferroelectricity and ferromagnetism leading to magnetically controlled electrical polarization and vice versa, started to pique interest during the 1950s through soviet research. After rather expendable results in the early hours of research it took ten years until first notable magnetoelectric coefficients were measured. Since the 1990s, the number of publications including the word "magnetoelectric" in their keywords is steadily growing, leading to the discovery of more and more materials exhibiting the effect. With growing possibilities, also the field of potential applications were expanding, covering the whole spectrum from sensoric and actuatoric systems to applications in spintronic systems.[11] Magnetoelectric materials may be divided into two general groups. Single phase magnetoelectric multiferroics show an intrinsic ME effect, caused through the linear magnetoelectric coupling constant, which can be derived from the free energy of a single-phase crystal as follows (Equations take use of Einstein notation):

$$F(\vec{E},\vec{H}) = F_0 - P_i^s E_i - M_i^s H_i - \frac{1}{2}\epsilon_0\epsilon_{ij}E_iE_j - \frac{1}{2}\mu_0\mu_{ij}H_iH_j - \alpha_{ij}E_iH_j - ... \quad (1.1)$$

With F being the free energy, $\vec{E}$ and $\vec{H}$ the electric field strength and the magnetic field strength respectively, P^s the spontaneous electric polarisation, M^s the spontaneous magnetisation, ϵ and μ the electric and magnetic susceptibility and with α denoting the magnetoelectric coupling constant. Finding the first derivatives with respect to E and H of Formula 1.1, leads to the electric polarisation

$$P_i(\vec{E},\vec{H}) = -\frac{\delta F}{\delta E_i} = P_i^s + \epsilon_0\epsilon_{ij}E_j + \alpha_{ij}^{EM}H_j + ... \quad (1.2)$$

and the magnetisation

$$M_i(\vec{E},\vec{H}) = -\frac{\delta F}{\delta H_i} = M_i^s + \mu_0\mu_{ij}H_j + \alpha_{ij}^{ME}E_i + ... \quad (1.3)$$

As can be seen in Equations 1.2 and 1.3, the linear magnetoelectric coupling constant α links the electric polarisation P with the magnetic field strength H as well as the magnetisation M with the electric field strength E. From general energy considerations, we see that the coefficients α^{ME} and α^{ME} are symmetrical and thus the effect has equal strength in both directions. Equation 1.1 does not end at the linear magnetoelectric term but also includes some higher ordered non-linear magnetoelecric constants β and γ, which were not considered here as their contribution to the actual effect is extremely small. Usually if mentioned, the magnetoelectric effect refers to the linear magnetoelectric constant α. On the other hand, there are magnetoelectric composite materials. A layered structure of piezoelectric and magnetostrictive or piezomagnetic and piezoelectric phases can lead to high magnetoelectric coupling constants. Crucial parameters of quality are the ferroic properties of the single phases as well as the coupling between them.[12]

1.2.2 Fields of application for magnetoelectric materials

The possibility to directly combine the magnetic and electric properties of materials opens up a whole new degree of freedom in material design and will be an important part in future research. Especially in times when miniaturisation, power saving and energy harvesting are driving factors, magnetoelectrics have the potential to be part of ground breaking developments. The biggest driver behind the research on multiferroic magnetoelectrics might nowadays be the spintronic industry as these materials bring additional functionalities to multiple stage memory devices and gate controlled magnetic memories.[13] Further applications can be found in sensoric and actuatoric devices, transformers using the magnetoelectric voltage gain effect,[14] microwave devices[15] and ME memories.[16] Since industrial applications of magnetoelectrics usually are operating at room temperature or at least in an acceptable range around it, many materials which show magnetoelectric behaviour only at very low temperatures are unviable. Bismuth Ferrite on the other hand, expresses ME behaviour up to temperatures well above room temperature, thus again emphasising the applicability of single phased BFO again.

1.3 The Perovskite Structure

The perovskite structure, named after the calcium titanium oxide mineral perovskite $CaTiO_3$, is commonly found in chemical compounds with the general formula ABX_3. A and B describe cations which are coordinated by corner linked octahedra of the X-anions. The B-cation is sitting in the center of these octahedra which form a three dimensional network. In the resulting cuboctahedral gaps the A-cation is placed, resulting in an twelve-fold X-coordination of it. This description is valid for the ideal, not distorted perovskite structure, the aristotype with point group $Pm\overline{3}m$. A famous representative of this structure is $SrTiO_3$. The BX_6 octahedra show no tilting. Variations in the cation size cause distortions and tilting of these octahedra, leading to changes in coordination number and different morphologies of the coordination polyhedra. Alongside with cation displacements enabling polar structures, the octahedral distortion and tilt in perovskites are crucial parameters affecting the electric and magnetic properties of the compounds. The appearance of perovskites in different crystal systems is also attributable to these distortions.[17] Octahedral tilting in perovskites can be described with the Glazer notation.[18] The many possibilities of adaption allow an enormous number of compounds appearing in the perovskite structure. One way to estimate the magnitude of distortion is given by the Goldschmidt tolerance factor

$$t = \frac{r_A + r_X}{\sqrt{2}\,(r_B + r_X)} \tag{1.4}$$

In equation 1.4, $r_{A/B/X}$ stands for the ionic radii of the involved cations (A, B) and the anion X. The ideal perovskite structure with space group $Pm\bar{3}m$, geometrically exists with a value of $t = 1$. Effectively, the $Pm\bar{3}m$ structure is observed for values $0.89 < t < 1$. Distorted perovskite structures appear when $0.8 < t < 0.89$, values below 0.8 lead to the formation of ilmenite structure. Compositions with $t > 1$ will exhibit hexagonal symmetries. Though, the Goldschmidt tolerance factor is only one criterion describing the possible structure of a perovskite. As mentioned, the aristotype of the perovskite structure possesses the $Pm\bar{3}m$ space group symmetry. This is the structure with the highest possible symmetry of a perovskite and all other structures are derived from it. They are then called hettotypes. By definition, these hettotypes have a lower symmetry than the aristotype. A way to show such group-subgroup relationships between crystal structures are Bärnighausen family trees.

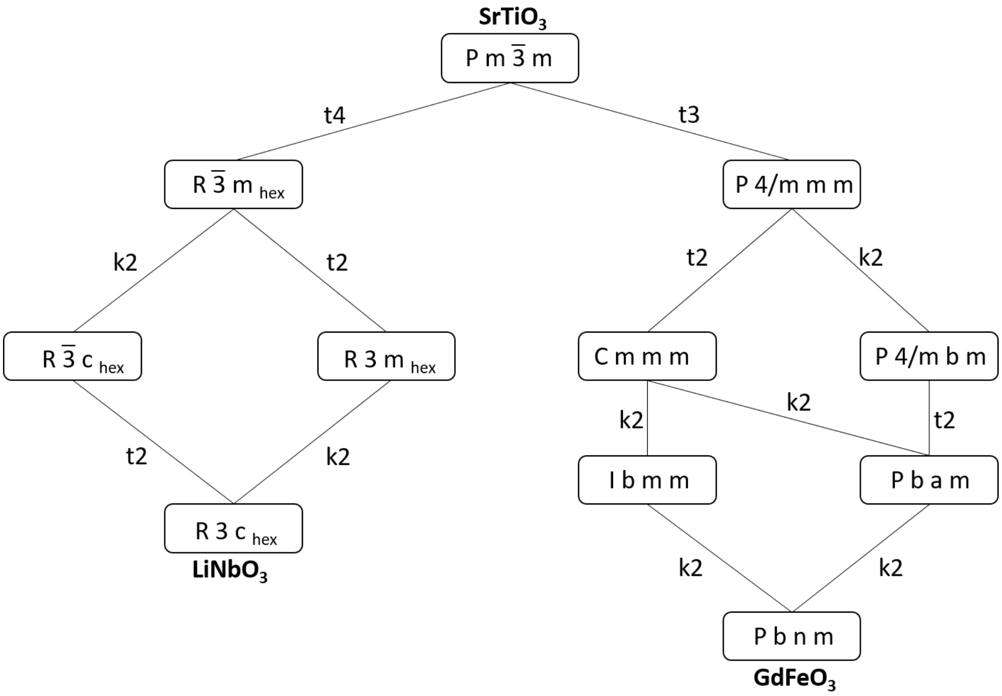

Figure 1.3: Bärnighausen family tree showing the group-subgroup relations or the perovskite aristotype and the crystal structures of α-BFO ($R3c$) and β-BFO ($Pbnm$).

Figure 1.3 shows such a Bärnighausen tree, depicting the group-subgroup relations of the aristotype $Pm\bar{3}m$. Subgroups are directly connected with lines to their supergroups, the factor of symmetry reduction indicated by the number next to the line. The letters t and k are an indication of if the subgroup is translationengleich or klassengleich to its supergroup. As can be seen, the space group of α-BFO, $R3c$, and the space group of β-BFO, $Pbnm$, are in no direct group-subgroup relationship. Thus, phase transitions between these two space groups must be of first order.[19] The relations between the perovskite aristotype $Pm\bar{3}m$ and the space groups of α- and β-BFO is shown in Figure 1.4.

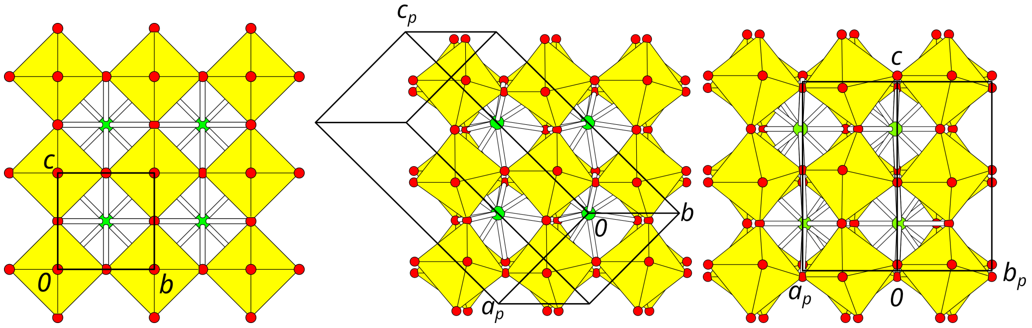

(a)

(b)

(c)

Figure 1.4: (a) The $Pm\bar{3}m$ aristotype structure viewed down [100]. (b) Distorted perovskite structure of α-BFO with hexagonal unit cell viewed down [42$\bar{1}$]. (c) Distorted perovskite structure of β-BFO with orthorhombic unit cell viewed down [110].

The structure which can be seen in Figure 1.4(a) is the aristotype as the yellow octahedra are not distorted and built up in a regular lattice. Figure 1.4(b) shows the hexagonal $R3c$ unit cell placed in the distorted perovskite structure. The orthorhombic $Pbnm$ unit cell is placed in the distorted perovskite structure in Figure 1.4(c).

1.4 Bismuth Ferrite $BiFeO_3$

BFO is typically synthesized through sintering stoichiometric mixtures of Bi_2O_3 and Fe_2O_3.[20] Its phase diagram was object of investigation of multiple research groups and still shows some ambiguities.

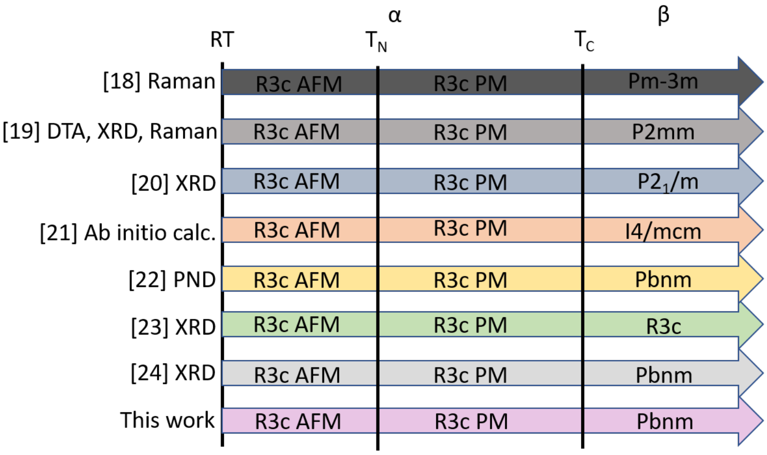

Figure 1.5: Different approaches to determine the crystal structure of the paraelectric β-phase

Figure 1.5 gives a comparison between selected approaches to determine the crystal structure and symmetry of the α-phase and the paraelectric β-phase of BFO. The stability range of the α-phase is divided into two regions. The antiferromagnetic region below the Neél temperature of $T_N \sim 370°C$ and the paramagnetic region above the Neél temperature until the Curie Point at $T_C \sim 822°C$. These high ordering temperatures allow the expression of magnetoelectricity at a suitable temperature range including room temperature, which is essential for the widespread aplicability in technological applications. In all publications referred to in Figure 1.5, the α-phase is accepted to appear in a rhombohedral $R3c$ perovskite structure with its hexagonal lattice parameters $a_{hex} = 5.58$Å and $c_{hex} = 13.87$Å and its pseudocubic unit cell parameters $a_{rh} = 3.89$Å and $\alpha_{rh} = 89.3°$,[28] where $[111]_{rh} = [001]_{hex}$.[26] Regarding the β-phase, several different approaches were used to determine its crystal symmetry and also multiple structures were proposed. Raman spectroscopy studies done by Haumont et al.[21] in 2006 suggest $Pm\bar{3}m$ symmetry, Raman spectroscopy combined with Differential Thermal Analysis (DTA) and X-ray diffraction studies conducted by Palai et al.[22] in 2008 propose $P2mm$. Another study done by Haumont et al.[23] in 2008, this time XRD only, suggested $P2_1/m$ as the β-phases appearance. Ab initio calculations of Kornev et al.[24] predict $I4/mcm$, Powder Neutron Diffraction (PND) studies by Arnold et al.[25] propose $Pbnm$ and XRD studies by Selbach et al.[26] suggest $R3c$, the same structure as the α-phase. Figures 1.6 and 1.7 show stereoscopic images of the crystal structures of the α and the β phase of BFO respectively. The bismuth atoms with their coordination polyhedra are purple, iron atoms and coordination polyhedra are brown. Oxygen atoms are depicted in red. The structures were created with VESTA.[29] The $Pbnm$ setting was chosen for the representation of the β-phase due to the findings of Arnold et at. and Wei et al. and also owing to the findings of this work, which also clearly suggest $Pbnm$ as the β-phases symmetry. One reason of the very different outcomes is the thermal instability of BFO at elevated temperatures. Volatility of Bismuth leads to the formation of non-perovskite secondary phases with not-negligible phase fractions, complicating the accurate determination of phases.[30] In recent XRD studies of Wei et al., this problem was noticed and counteracted by doping BFO with 5% Lanthanum. As opposed to doping with other rare earth materials or transition metals, doping with Lanthanum does not introduce changes of the low temperature crystal symmetry, nor does it change the Curie point of BFO while it stabilizes the material at higher temperatures avoiding the formation of unwanted secondary phases. Considering this, the results of Wei et al with Lanthanum doped BFO, which also suggest an orthorhombic β-phase in $Pbnm$ setting might be an interesting benchmark for the characterisation of the β-phase of BFO.[27] This phase change from the rhombohedral α-phase to the orthorhombic β-phase is accompanied by a sudden volume contraction and corresponds to the ferroelectric-paraelectric phase transition as well. The β-phase exists up to approximately $890°C$, where it transforms into the cubic γ-phase.[25] Due to polar displacements of the Bi and the Fe atoms along the $[111]_{rh}$ direction, BFO shows ferroelectric polarization along this threefold axis,[31] which, as rather recent experiments show, is high with values up to $P_{111} = 100\mu C/cm^2$.[32] Regarding the magnetic properties of BFO, different assumptions about the type and its origins were made. It seems pretty clear that BFO is a G-type antiferromagnet at room temperature, meaning that each magnetic moment is surrounded by six inter- and intraplanary opposed magnetic moments.[28] Through a ferroelectrically induced spin canting, the spins, and therefore the magnetic moments are not completely opposing each other, but show a non-linearity angle of about 1°. This canting angle should result in a small macroscopic magnetization of about $M = 0.05\mu_B$ per unit cell.[33] Superimposed on the antiferromagnetic spin structure, lies a spin cycloid with an approximate periodic length of $l_{cyc} = 620Å$. This means that the antiferromagnetic spins show a rotation of 360 degrees within l_{cyc}, cancelling out the before described magnetization completely. Surpressing this spin cycloid leads to weak ferromagnetism.[34]

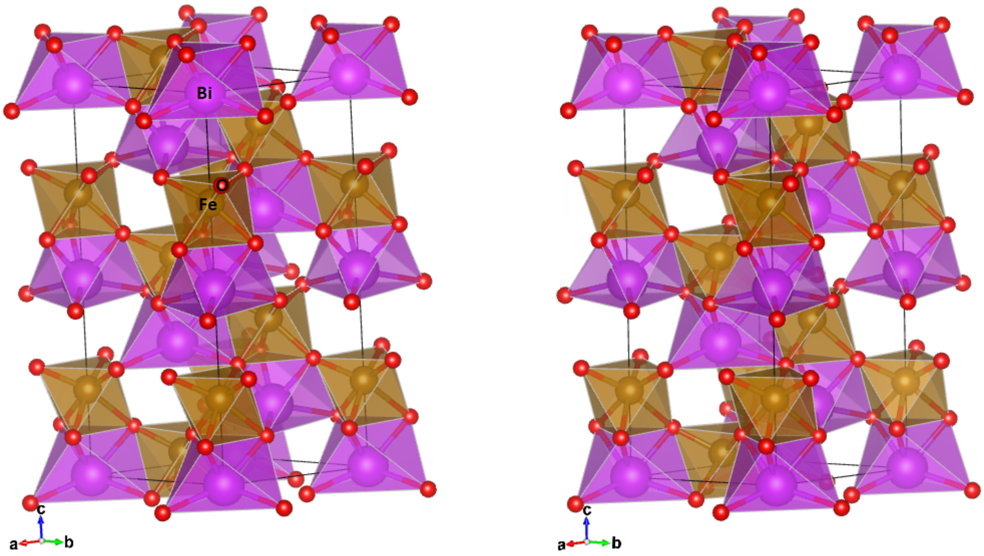

Figure 1.6: Stereo-image of the crystal stucture of α-BFO in $R3c$ setting.

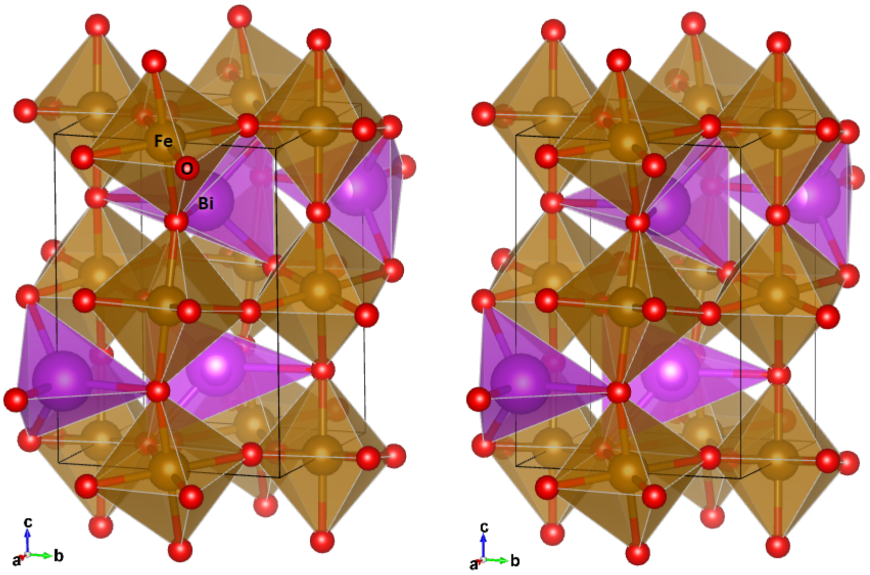

Figure 1.7: Stereo-image of the crystal stucture of β-BFO in $Pbnm$ setting.

2 Experimental Methods

2.1 Perturbed Angular Correlation (PAC)

The Perturbed Angular Correlation (PAC) method, like Mössbauer spectroscopy, is a method of nuclear physics taking advantage of hyperfine fields existing within the examined structure. There are three different specifications of PAC methods. The information can be derived from beta-gamma, electron-gamma and gamma-gamma coincidences. The PAC method used in this work makes use of the anisotropic emission of two γ quanta, being result of a nuclear decay of a probe atom present in a metastable state, to its ground state via a γ-γ cascade. The presence of magnetic fields or Electric Field Gradients (EFG) at the location of the probe atom causes hyperfine interactions with its nuclear moments, leading to a distortion of the probe atoms intermediate state. The following anisotropy of the γ emission gives information on the local structure of the probed sample. Properties, such as defects, nanostuctured surfaces and interfaces, phase transitions, magnetic and structural transitions as well as formation of participants may be analysed at the nanoscale.[35] As the probe atoms are implanted in the sample, the measurement variables become a more or less intrinsic component as they are directly influenced by the atomic structure surrounding them. This is one of the main differences to other measurement methods which take advantage of extrinsic measurement variables, like X-ray diffraction measurements (XRD).

2.1.1 Electric Quadrupole Interaction

As this work is primarily dealing with hyperfine interactions of electrical kind, focus will only be given on the Electric Quadrupole Interaction and its fundamental property, the electric field gradient. The EFG, being the traceless component of the second spacial derivative of the electrostatic potential within the atomic lattice, is a symmetric 3×3 tensor,

$$V_{ij} = \frac{\partial^2 V}{\partial x_i^2 \partial y_j^2}. \tag{2.1}$$

Through a coordination transformation to the reference coordinate system, the components of this tensor can be reduced to the three diagonal elements X_{xx}, V_{yy} and V_{zz}. The reference coordinate systems axes usually are set in a way such that the largest component of the tensor points in z-direction. With

$$|V_{zz}| \geqslant |V_{yy}| \geqslant |V_{xx}| \tag{2.2}$$

and the use of the Laplace equation

$$V_{zz} + V_{yy} + V_{xx} = 0, \tag{2.3}$$

its possible to completely describe the EFG with only two parameters, namely the largest component V_{zz} and the asymmetry parameter

$$\eta = \frac{V_{xx} - V_{yy}}{V_{zz}} \tag{2.4}$$

with possible values between 0 (axial symmetric) and 1 (asymmetric). Electric field gradients are strongly dependent on charge distributions. A perfect charge distribution as imagined through a theoretical cubic lattice will not cause an EFG because the charge distributions are spherically symmetric and isotropic. Thus, V_xx=V_yy=V_zz and as the trace of the tensor is zero, all components of the electric field gradient are zero, not contributing to an electric quadrupole moment. Local defects or non-cubic crystal systems may lead to a non-vanishing EFG. The interaction between the EFG and the probe nucleus' quadrupole moment Q leads to a hyperfine splitting of the sensitive intermediate states energy level I into magnetic sublevels $M = \pm I, \pm(I-1), \pm(I-2), ...$ with energies calculated through

$$E_Q(M) = \frac{3M^2 - I(I+1)}{4I(2I-1)} eQV_{zz} \tag{2.5}$$

with $e = 1.6021 * 10^{-19}$C being the electron charge. Thus the energy between two sublevels M and M' calculates through

$$E_Q(M) - E_Q(M') = \frac{3eQV_{zz}}{4I(2I-1)}(M^2 - M'^2) = 3(M^2 - M'^2)\hbar\omega_Q \tag{2.6}$$

with $\hbar = 6.5821 * 10^{-16}$eVs being the reduced planck constant and

$$\omega_Q = \frac{eQV_{zz}}{4I(2I-1)\hbar} \tag{2.7}$$

being the quadrupole interaction frequency. With a symmetric EFG, meaning that $\eta = 0$, and an intermediate state energy level of $I = 5/2$, transition frequencies of $\omega_1 = 6\omega_Q$, $\omega_2 = 12\omega_Q$ and $\omega_3 = \omega_1 + \omega_2$ occur. If $\eta \neq 0$, the sublevel energies dependend on η and generally can not be solved analytically. However, for probe nuclei with intermediate levels of $I = 5/2$, a calculation is possible through the following equations:

$$E_{\pm 5/2} = E_0 + 2\alpha\hbar\omega_Q \cos\left(\frac{1}{3}\arccos(\beta)\right) \tag{2.8}$$

$$E_{\pm 3/2} = E_0 - 2\alpha\hbar\omega_Q \cos\left(\frac{1}{3}\left(\pi + \arccos(\beta)\right)\right) \tag{2.9}$$

$$E_{\pm 1/2} = E_0 - 2\alpha\hbar\omega_Q \cos\left(\frac{1}{3}\left(\pi - \arccos(\beta)\right)\right) \tag{2.10}$$

with

$$\alpha = \sqrt{\frac{28}{3}(3 + \eta^2)} \ \text{ and } \ \beta = \frac{80(1 - \eta^2)}{\alpha^3} \tag{2.11}$$

Of course, owing to the dependence of sublevel energies on η, likewise the angular transition frequencies ω_n become dependent on η.

$$\omega_1 = E_{\pm 3/2} - E_{\pm 1/2} = 2\sqrt{3}\alpha\omega_Q \sin\left(\frac{1}{3}\arccos(\beta)\right) \tag{2.12}$$

$$\omega_2 = E_{\pm 5/2} - E_{\pm 3/2} = 2\sqrt{3}\alpha\omega_Q \sin\left(\frac{1}{3}\left(\pi - \arccos(\beta)\right)\right) \tag{2.13}$$

$$\omega_3 = \omega_1 + \omega_2 = 2\sqrt{3}\alpha\omega_Q \sin\left(\frac{1}{3}\left(\pi + \arccos(\beta)\right)\right) \tag{2.14}$$

Figure 2.1 shows the dependence of the sublevel energies and of the angular transition frequencies on η. Whereas with $\eta = 0$ the transition frequencies ratio $\omega_1 : \omega_2 : \omega_3$ is $1 : 2 : 3$, this ratio changes in the case of $\eta \neq 0$ which can be seen in Figure 2.1.

Thus these transition frequencies are unique for the description of the strength and also the symmetry of the electric field gradient present at the probe nucleus.

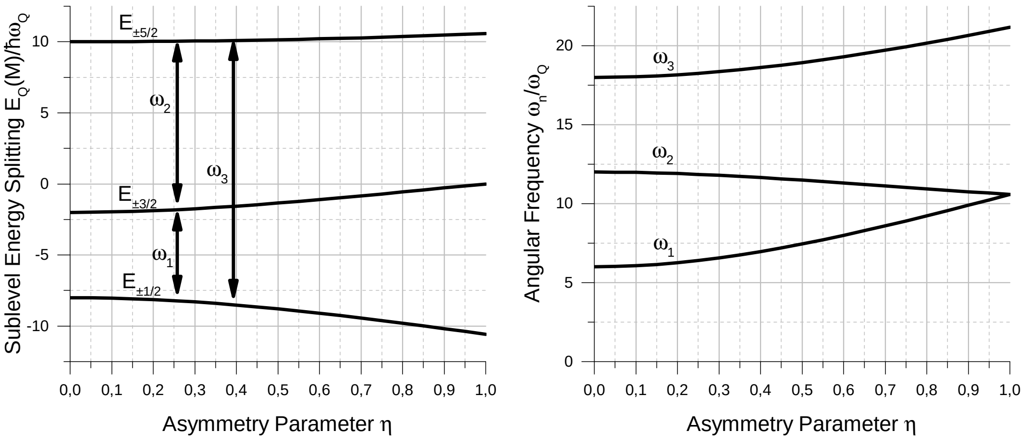

Figure 2.1: Change of sublevel energies $E_Q(M)$ with increasing asymmetry parameter and resulting change of angular frequencies ω_n calculated with Equations 2.8-2.14. Reference value of $\omega_Q = 10$ Mrad/s, valid only for $I = 5/2$.

2.1.2 Theory of Perturbed Angular Correlation

As already mentioned, the fundamental principle of PAC is the detection of the angular correlation between two consequent γ quanta originating from the same nucleus through radioactive decay. The nucleus decays from an excited state characterized by its spin I_i and its magnetic quantum number M_i to its ground state (I_f, M_f). This loss of energy takes place via an intermediate level (I, M) with non-vanishing lifetime, shown in Figure 2.2(a). Owing to the conservation of angular momentum and following selection rules

$$|I_i - I| \leq l \leq I_i + I \;\text{ and }\; M_i - M = m \tag{2.15}$$

where l is the angular momentum and m is the magnetic quantum number of the emitted photon the characteristic of emission of both γ quanta is described. Depending on the quantum numbers of the different energy levels, l and m of γ_1 and γ_2 are predetermined. As shown in Figure 2.2(b), the possibility of emission of a photon in direction of the nucleus spin I at the moment of ejection depends on the photons angular momentum l and magnetic quantum number m.

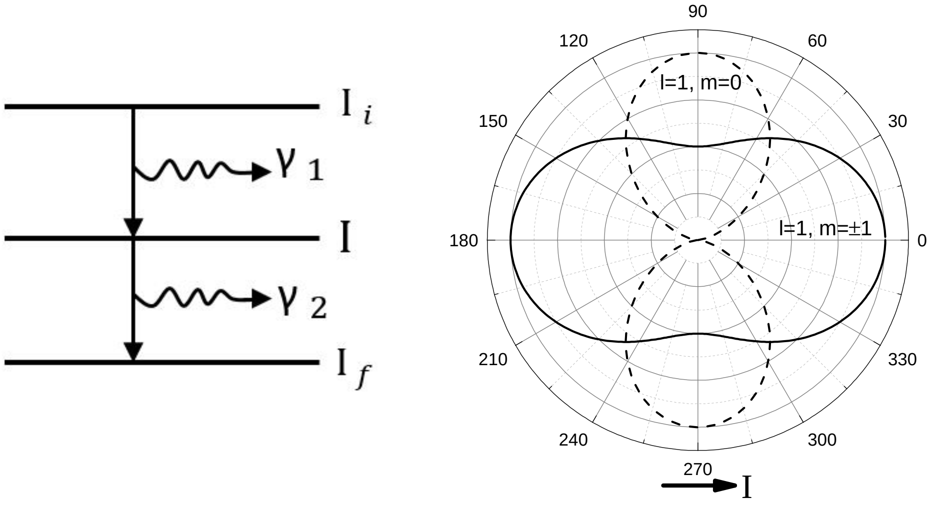

(a) (b)

Figure 2.2: (a) γ-γ cascade decay from an excited state with spin I_i to the ground state I_f via an intermediate state I. (b) Angular characteristic of dipole radiation with $l = 1, m = 0$ (dashed line) and $l = 1, m = \pm 1$ (solid line). Spin I in horizontal direction.

According to this reasoning, one could expect that the spherical angular distribution is anisotropic by nature. However, as the nuclear spins of a conglomerate of atoms are orientated randomly in an unpolarized sample, the macroscopic angular distribution is isotropic. One way to overcome this is to set a hypothetical reference axis in direction of the firstly detected γ_1 photon. By doing so, a subset of atoms, with their spin pointing in this direction is selected. With this knowledge, the corresponding second gamma γ_2, identified through its energy occurring with an exact delay of the intermediate states lifetime, is not ejected isotropically anymore. The angular correlation function $W(\theta)$, describing the probability of detecting γ_2 within an angle θ with respect to γ_1 calculates through

$$W(\theta) = \sum_{k=0}^{k_{max}} A_{kk} P_k \left(\cos\theta\right), \tag{2.16}$$

whereby k, owing to conservation of parity, only adopts even values and A_{kk} are angular correlation coefficients describing the deviation of coincidence probability compared to an isotropic case with $W(\theta) = 1$. Exact values of A_{kk}, which are dependent on the multipolarity of the γ radiation and the nuclear spin, may be taken from literature like [36]. The running index k can take even values between $0 \leq k \leq$Min$[2I, 2l_{\gamma1}, 2l_{\gamma2}]$ and $P_k(cos(\theta))$ are the associated Legendre polynominals. Figure 2.2(b) shows the angular distribution of a photon with spin L=1. The angular correlation function between the two consecutive γ quanta can be measured with two or more detectors. A very basic installation is shown in Figure 2.3 with a fixed detector 1 measuring γ_1 and thus defining the reference axis and a movable detector 2 detecting γ_2. The measured angular correlation function $W(\theta)$ is also schematized in Figure 2.3, showing the lower emission-probability at an angle of 90°.

Setups used to conduct PAC measurements usually consist of four or six fixed detectors arranged in angles of 90° and 180° to each other. If electromagnetic fields are present at the probe nucleus site, its nuclear spin will experience a torque, leading to a spin precession around the field direction with an angular frequency ω, proportional to the field strength. In the case of interactions of magnetic nature, this spin precession is called Larmor precession and the angular frequency is the so called Larmor frequency ω_L. Electric quadrupole interactions, described in Section 2.1.1 lead to a spin precession with the derived angular frequencies ω_n. The interaction between the nuclear moments with the surrounding fields during the lifetime of the intermediate state leads to a mediation of the transitions between the different M substates, again having effect on m and thus the angular distribution of γ_2.

This spin precession expresses itself through a time dependent perturbation func-

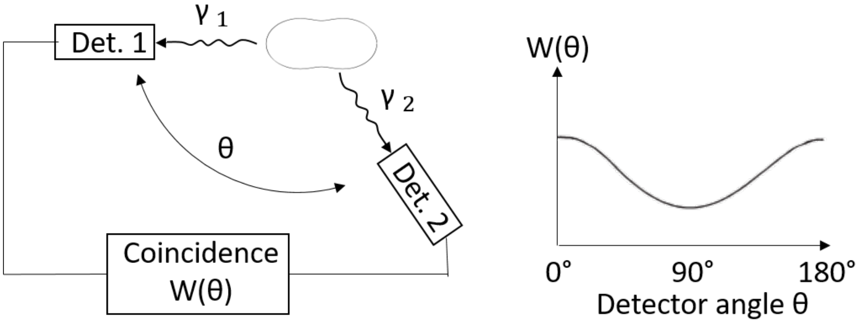

Figure 2.3: Change of sublevel energies $E_Q(M)$ with increasing asymmetry parameter and resulting change of angular frequencies ω_n calculated with Equations 2.8-2.14. Reference value of $\omega_Q = 10$ Mrad/s, only valid for $I = 5/2$.

tion $G_{kk}(\eta, t)$ which modifies the angular correlation function 2.16 to

$$W(\theta, t) = \sum_{k=0}^{k_{max}} A_{kk} G_{kk}(\eta, t) P_k (\cos(\theta)) \tag{2.17}$$

$G_{kk}(\eta, t)$, though only in the case of $I = 5/2$ and electrostatic interaction, can be described as a linear combination of cosine functions based on the transition frequencies calculated with Formulas 2.12-2.14:

$$G_{kk}(\eta, t) = \sum_{n=0}^{3} s_{kn}(\eta) \cos (\omega_n(V_{zz}, \eta)t) \tag{2.18}$$

with $s_{kn}(\eta)$ being the coefficients of the cosine terms. The exact values can also be found in other literature like Friedsam.[37]

2.1.3 Data Acquisition and Computing

In the observable signal, the angular correlation function is combined with the natural decay curve of the radioactive nucleus. The point of interest of the method is the perturbation function $G_{kk}(\eta, t)$ with its cosine terms of the transition frequencies ω_n describing the hyperfine interaction at the probe nucleus. During measurement, two fixed detectors with an angle of usually either 90° or 180° to each other create a coincidence spectrum

$$N(\theta, t) = N_0 e^{\frac{-t}{\tau}} W(\theta, t) + C \tag{2.19}$$

showing the lifetime curve of the probe nucleus modulated with the angular correlation function $W(\theta)$. τ is the lifetime of the intermediate state, N_0 is the counting rate (sample activity) at $t = 0$ and C describes a time independent background counting rate arising from random correlations. Simplifying Formula 2.17 with $k_{max} = 4$ but neglecting A_{44}, since its value is significantly smaller than A_{22}, leads to

$$N(\theta, t) = N_0 e^{\frac{-t}{\tau}} \left(1 + A_{22} G_{22}(t) P_2 \left(\cos(\theta)\right)\right) + C. \tag{2.20}$$

The chosen angles between the detectors simplify the calculation of the so called $R(t)$ value, as $P_2 (\cos(180°)) = 1$ and $P_2 (\cos(90°)) = -1/2$, the lifetime term can be eliminated from the equation leading to

$$R(t) = 2 \frac{N(180°, t) - N(90°, t)}{N(180°, t) + 2N(90°, t)} = A_{22} G_{22} \tag{2.21}$$

with A_{22} known and G_{22} being the pure perturbation function. This simplification is valid for an intermediate state energy level of $I = 5/2$.[38] The first steps in experimental data analysis were a time stamp fit of all 30 coincidence spectra (six detector setup: 24 90°-spectra and 6 180°-spectra) with the Interlude[39] software, which in principle evaluates Formula 2.21. Now, as the perturbation function was extracted, a theoretical fit function $G_{fit}(t)$ which is a linear combination of multiple perturbation functions $G_i(t)$ in the form of

$$G_{fit} = \sum_i f_i G^i_{kk}(\eta, t) = \sum_i f_i \sum_{n=0}^{3} s^i_n(\eta^i) \cos\left(\omega^i_n(V^i_{zz}, \eta^i) t\right) e^{-\delta^i \omega^i_n t}, \tag{2.22}$$

weighted by respective fractions f_i with the normalisation condition $\sum_i f_i = 1$.[40] As the lattice never is perfect and the probe environments will slightly differ from each other, the EFG is distributed around a mean value of the interaction frequency ω_n. This Lorentzian distribution causes an exponential damping of the perturbation function and the parameter δ describes the full width at half maximum (FWHM) width of this Lorentz distribution. Ordered structures typically show small values of δ whereas unannealed samples directly after the probe implantation may show strong damping due to implantation damage and the probe nuclei not being at their preferred final position. The final fit then was realized with GFIT19, a modified version of the NNFit software package.[41]

2.1.4 PAC spectroscopy at CERN - The ISOLDE Facility

Since the mid 1970s, Perturbed Angular Correlation is a standard technique in Solid State Physics (SSP) research at the ISOLDE (Isotope Separator On Line DEvice) facility of the European Organisation for nuclear Research (CERN). ISOLDE, located in the heart of CERN´s accelerator complex, uses protons with high energies up to 1.4GeV from the Proton Synchotron Booster (PSB) to generate radioactive ion beams via spallation, fragmentation and fission reactions between the protons and the target atoms.[42] Through different target marterials used for the ion generation, a variety of radioactive ions may be delivered in high purity with the help of the Resonant Ionisation Laser Ion Source (RILIS) and two mass separator devices (GPS and HRS). The General Purpose Separator (GPS) device with a mass separation of $M/\Delta M = 2400$, feeds two beam line outlets of which one, namely the GLM (General Low Mass) beamline is used for SSP experiments.[43, 44]

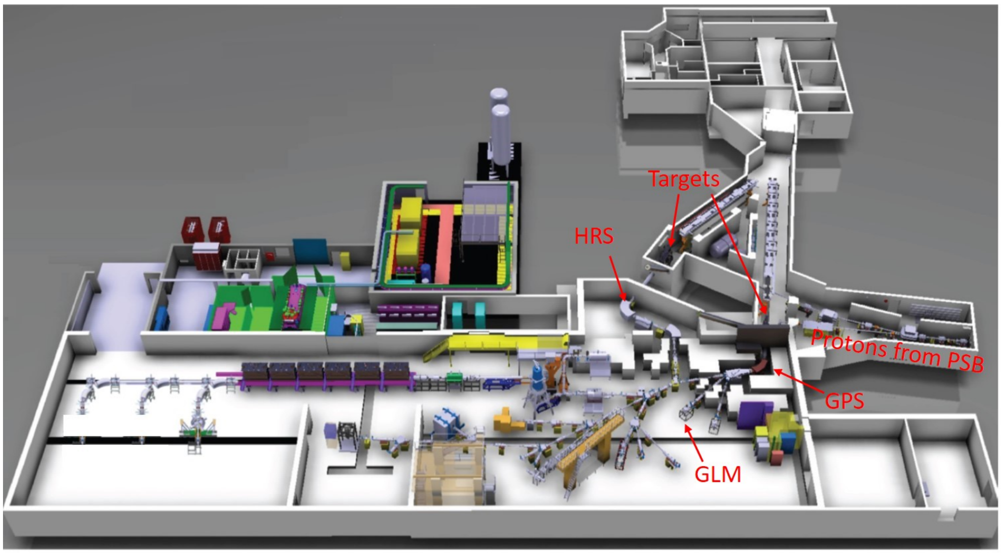

Figure 2.4: Overview of ISOLDE facility with the incoming protons, targets, mass separators and the used GLM beamline indicated.

2.2 X-Ray Diffractometry (XRD)

Compared to the Perturbed Angular Correlation Method, X-Ray Diffractometry measurements are of a macroscopic nature. The combination of both methods convinces by the possibility to inspect the phase purity as well as the crystal structure also from a more general point of view. XRD uses the phenomenon of coherent scattering of x-rays by periodic structures and the caused arising of interference patterns

2.2.1 X-rays

X-rays, like γ-rays or visible light, are electromagnetic waves and therefore photons. With wavelengths λ in the range of inneratomic distances, so between 10^{-3} to 10^{1}nm, x-rays have a higher energy than visible light, but are lower in energy than γ-rays. In typical diffraction measurements, electron acceleration energies of up to 100keV are common whereas special irradiation techniques may use energies up to 400keV. X-rays are produced with the help of x-ray tubes through the deceleration of accelerated electrons in a target material. Through this process, a spectrum consistent of two main constituents is created. The so called bremsspectrum is a continuous spectrum with a minimum wavelength λ_0.

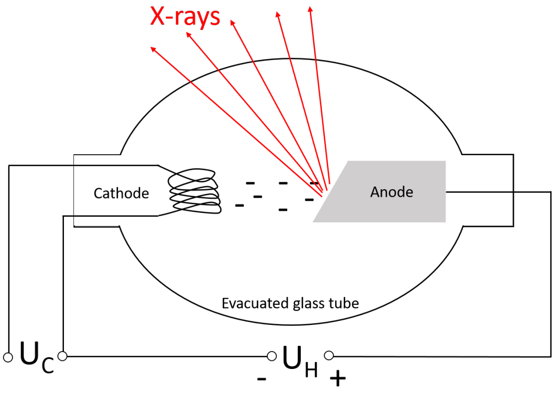

Figure 2.5: Schematic view of a x-ray tube. The anode often is water cooled to dissipate the created thermal energy when electrons are decelerated.

Through interactions with the Coulomb field of the target atoms, the momentum of electrons is reduced leading to the emission of photons. λ_0, the shortest wavelength able to be produced by an x-ray tube is assigned to the stopping of an electron with its velocity v in just one step, converting all its kinetic energy into x-ray radiation. It depends on the energy of the impinging photons which is determined by the acceleration voltage. Figure 2.5 shows a schematic of a x-ray tube. The evacuated glass tube contains a cathode, which typically is an electrically heated tungsten filament producing electrons, and an anode made of the material creating the desired characteristic x-ray spectrum. The anodes mostly are watercooled to allow a fast dissipation of the huge energy amounts created during the electron stopping processes. In order to accelerate the electrons created by the cathode towards the anode material, large DC voltages are applied between anode and cathode. The impinging electrons are focused on the focal spot of the anode, leading to bremsstrahlung and characteristic x-ray radiation emission. Characteristic emission is caused by the ionisation of anode material atoms through the impinging electrons. When core electrons are ejected from their orbitals, electrons of higher energetic orbitals may take their place leading to the emission of the energy difference through a photon.

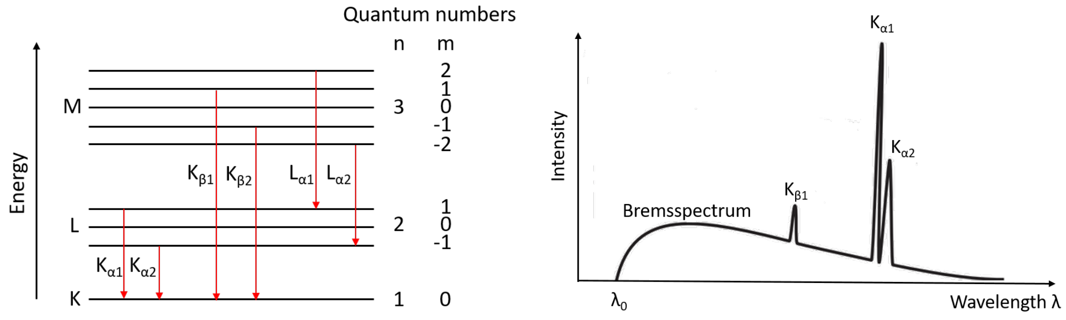

(a) (b)

Figure 2.6: (a) Energy levels and allowed transitions shown for $n \leq 3$. (b) Typical x-ray spectrum showing the combination of the continuous bremsspectrum with the discrete characteristic emissions $K_{\beta 1}$ and the K_α doublet.

As the selection rules only allow certain jumps between energy levels, namely $\Delta n \neq \pm 0$ and $\Delta m = \pm 1$ (shown in Figure 2.6(a)), the quantum energy differences are characteristic for each element and so lead to a discrete spectrum which is called a line spectrum. Characteristic energies are named after the lowest energy level included in the transition (K, L,...). The lower-case greek appendix describes the second included energy level. In this case α describes a transition from the next higher energy level and β describes a transition starting from the after next level. The most energetic characteristic x-ray radiation is always the K-radiation, which appears as doublets of the higher energetic $K_{\beta 1}/K_{\beta 2}$ and $K_{\alpha 1}/K_{\alpha 2}$ (Figure 2.6(b)). In XRD experiments, depending on the desired wavelength, the K-radiation of the metals Cr, Fe, Co, Ni, Cu, Ag and Mo is used.

2.2.2 Theory

The most basic principle of XRD is the so called Bragg equation (Equation 2.23) which sets a relation between the wavelength λ of the x-rays, the beams incidence angle θ and the spacing between lattice planes d_{hkl}.

$$n\lambda = 2d_{hkl}sin(\theta) \tag{2.23}$$

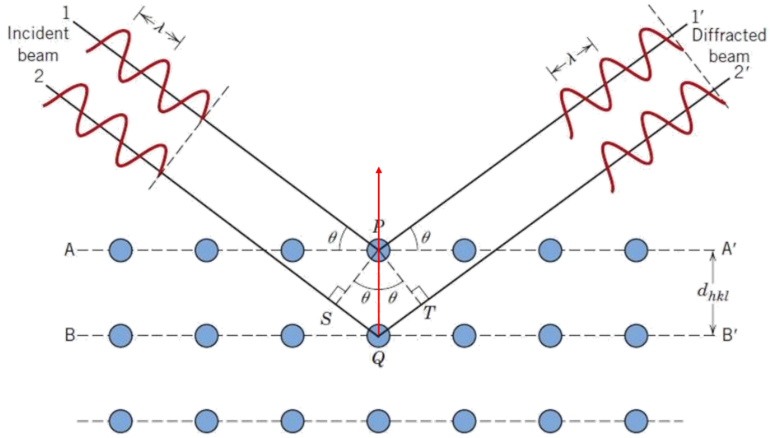

Figure 2.7: Diffraction of x-rays at the lattice plane hkl.

With a fixed wavelength (monochromatic radiation) and variation of the diffraction angle, specific interference patterns which are unique for different crystal structures arise. Figure 2.7 depicts a comprehensible graphical derivation of Bragg´s law. This description is simplified. It does explain the positions of the reflections but not their intensities. Also the reflection on only two lattice planes as seen in Figure 2.7 is simplified and would not give a discrete diffractogram. For a discrete diffractogram an infinity of lattice planes is necessary. Constructive interference only occurs when the diffracted waves have the same phase. Thus the path difference $2d_{hkl}\sin(\theta) = \mid SQ \mid + \mid QT \mid$ between the incident beams 1 and the diffracted beam $1'$ and the incident beam 2 with its diffracted beam $2'$ must be a integer multiple n of the x-ray wavelength λ. Diffracted x-rays and followed interferences within a specific diffraction angle can thus be assigned to the atomic spacing of a material with a regular ordered atomic structure. Depending on the Miller indexes hkl which specify the orientation and spacing of the "reflecting" lattice plane, the lattice parameters can be calculated. For a cubic unit cell for example, the relation between the atomic layer spacing d_{hkl} and the lattice parameter a is given through

$$d_{hkl} = \frac{a}{\sqrt{h^2 + k^2 + l^2}}. \tag{2.24}$$

Crystal structures with lower symmetries show more complex relationships. Formulas can be derived using the metric tensor and are found in literature as Graef.[45] Typical XRD experiments are conducted with monochromatic x-ray radiation of small linewidth in order to maximize the angular resolution. The scattering angle is varied and the intensities of the reflections is detected. Through the angular positions of the reflections, the lattice plane spacing can be calculated by Bragg´s law. X-Ray Diffraction measurements can be done in different ways, on single crystals, polycristalline materials, through powder diffraction or on bulk material. Additionally, there are different geometries of the source-sample-detector arrangement. The used method in this work was powder and bulk diffractometry in Bragg-Brentano θ-θ arrangement, which means that the sample stays horizontally in the center of the x-ray source and the detector, which both rotate along a circle. Figure 2.8 shows a schematic view of this geometry. As the angle of incoming and outgoing radiation are altered simultaneously, the radius of the focussing circle becomes smaller with increasing angle θ. As the sample is not moving and thus can not be adjusted to this change, it is not uniformly focussed during the measurement. If the line focus of the beam is reduced, the angle-resolution can be improved with losses in intensities. Also the irradiated surface of the sample changes with the change of source and detector position. At lower angles θ, through geometric relations, the beam is covering a larger area of the sample. Though, the penetration depth of the photons is smaller. With growing angles θ, the areal beam covering of the sample will decrease but the penetration depth will increase. So, if the sample is thick enough, the irradiated sample-volume stays nearly constant over the range of diffraction angle θ. Of course this behaviour is depending on the atomic number of the elements present in the sample.

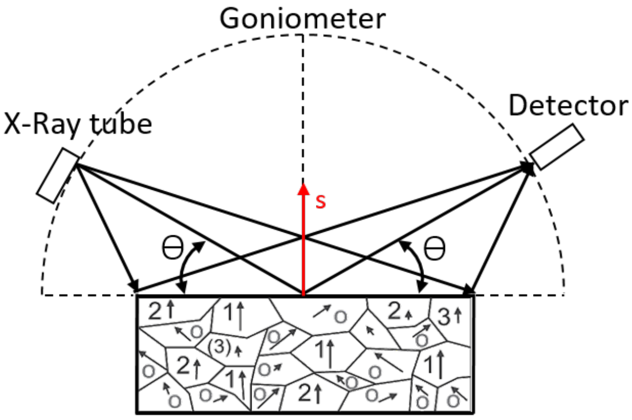

Figure 2.8: Bragg-Brentano θ-θ geometry with the incident x-rays from the xray tube to the left and the detector to the right. Diffraction vector **s** in red.

The advantage of having the sample in form of a powder becomes evident when the process is compared to single crystal diffraction. In Figure 2.8 heavily enlarged detail of a powder is shown. The length of the arrows is a measure of the atomic layer spacing while the orientation of the arrows is normal to the crystal plane (hkl). Reflections only occur when the diffraction vector **s**, which bisects the angle between the incident and the diffracted beam (visible in Figures 2.7 and 2.8) is parallel to the lattice plane normal and Bragg's law is fulfilled. A diffractogram of the powder shown in Figure 2.8 hence would only show reflections of grains marked with numbers $1, 2$ and 3 as their orientation allows diffraction. Peaks of grains marked with 0 would not be visible. The enormous quantity of randomly orientated grains in a fine powder leads to sufficient amounts of grains that are orientated in a way such that diffraction is possible, independently of their reflecting lattice planes orientation. Thus in powder XRD the maximum amount of reflections can be achieved making it an accurate method to determine the crystalline phases and lattice constants.

2.2.3 Data Acquisition and Computing

Through the movement of the x-ray tube and the detector, wide diffraction angles in the range of about 2θ = 5-140° can be measured. The detector continuously records the diffracted x-ray intensities and the count rate for each step is recorded. Thus, a diffractogram with intensities for each measured angular point is created. The intensities of the single reflections are not only depending on the number of grains oriented in the preferred direction, but also are influenced by the location of the atoms in the unit cell as the following equation shows:

$$F_{hkl} = \sum_{\mathrm{i}} f_{\mathrm{i}} T_{\mathrm{i}} \mathrm{e}^{2\pi i (x_{\mathrm{i}} h + y_{\mathrm{i}} k + z_{\mathrm{i}} l)} \tag{2.25}$$

with f_{i} being the atomic scattering factor which is the Fourier transform of the electron density of the element, which is of course dominated by the elements atomic number as x-rays are scattered on the atom electron shell. i runs over all atoms of the unit cell. Oszillations of the atoms are considered through the so called Debye-Waller factor T_{i}. The Debye-Waller factor is governed by many parameters including the atomic mass, binding forces and temperature and can generally be described as the Fourier transform of a trivariate Gaussian distribution, describing the atomic displacement from their average position. Through that, not only thermal oszillations but also static disorder is described by the Debye-Waller factor. In 2.25, $x_{\mathrm{i}}, y_{\mathrm{i}}$ and z_{i} are the atomic coordinates and h, k, l are the Laue indices of the reflecting lattice plane. F_{hkl} is the so called structure factor and the scattered peak intensities I_{hkl} show the dependence

$$I_{hkl} \propto | F_{hkl} |^2 \, . \tag{2.26}$$

After data collection, the diffractogram is stored as a list of intensity values beginning at the start angle with values for every step until the stop angle in digital form. To correctly evaluate the measured data, some preprocessing and data conditioning might be needed, depending on the desired outcome. Typical effects which are corrected for are for example threshold effects through background radiation, noisy data which require data smoothing or the removal of the $K_{\alpha 2}$ peaks. Background radiation is caused by natural or external detected radiation, elastic scattered radiation from air or dust particles within the wave path or from the sample holder or inelastic scattering. The background level is typically subtracted from the diffractogram through the application of a polynominal adjusted background line in order to achieve net impulse heights independent of the background. Noisy data can be the result of an insufficient number of counts per measurement point, mostly caused by insufficient measurement times. Polynominal smoothing of the data or the application of low pass filters might reduce the negative effects of this phenomenon. In case a hardware monochromator is not available, if desired, the cut off of the $K_{\alpha 2}$ peak can be easily done mathematically through the so called Rachinger correction. Moreover, owing to high computing powers of modern computers, this is not a standard method anymore as the $K_{\alpha 2}$ peak is simply fitted by the XRD software too. After the corrections, the peak detection is performed. There is a multitude of mathematical methods to achieve a peak detection, though the principle of course is a comparison of intensities. Quantitative phase analysis is done with the method of Rietveld analysis which uses structural data of all involved phases. The structural data is refined to a point where the diffractogram can be fitted in a very accurate way to determine the quantitative presence of elements or phases as well as their crystallographic parameters.[46]

3 Experimental Details

3.1 Sample Preparation

The BFO samples were manufactured by Dr. Marianela Escobar at University Duisburg-Essen through a conventional mixed oxide solid state synthesis.[47] Bi_2O_3 and Fe_2O_3 in purities of 99,9% and 99,99% respectively were ground in stoichiometric ratios with small amounts of ethanol. After drying, the homogeneous mixture was calcinated at 820°C for three hours. To break up agglomerates, the calcinated powder was reground to achieve a fine powder which was then pressed into pellets with a diameter of 10mm and a thickness of about 1,3mm with an uni axial six ton hydraulic press. Following this procedure, the pellets, the so called green bodies, were sintered for six hours again at 820°C, reaching that temperature with a heating rate of 270°C/h. The samples were then shipped to ISOLDE and further prepared for ion implantation and measurements on site. Reduction into small pieces was achieved by thoroughly carving the BFO pellet with a diamond blade to achieve the desired sizes.

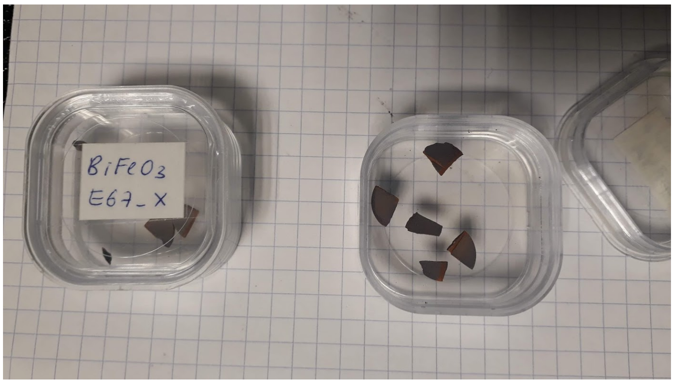

Figure 3.1: Cut samples ready for implantation. The grating of the paper in the background is 0,5cm.

3.2 The PAC probe - Cadmium isomer ^{111m}Cd

The probe nucleus of choice in our experiment is the radioactive Cadmium isomer ^{111m}Cd. Nuclear isomers are defined as nuclei which do not differ from their mother nucleus through their number of protons or neutrons, but are present in a different energy state. With an energy of $E_i = 396$keV and spin $I_i = 11/2$ in its exited state, the isomer loses its energy through a γ-γ decay with a half life of about $\tau_{1/2} = 48.54$min. After emitting γ_1 with an energy of $E_{\gamma_1} = 151$keV and angular momentum $L_1 = 6/2$, the nucleus reaches its intermediate state. The sensitive intermediate state with a spin of $I = 5/2$ offers a half life of $T_{1/2} = 84,5$ns, during which perturbations of the spin may be sensed, causing an anisotropic ejection of γ_2 with respect to γ_1 with an energy of $E_{\gamma_2} = 245$keV and $L_2 = 4/2$ to finally reach its ground state ^{111}Cd with spin $I_f = 1/2$.

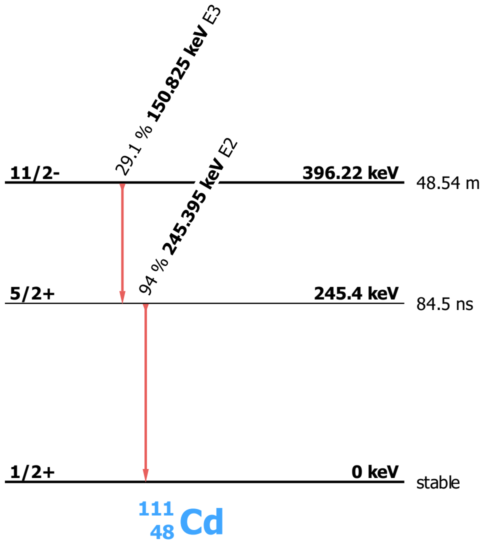

Figure 3.2: Decay scheme of ^{111m}Cd, created with the Nuclei software package.[48]

The production of ^{111m}Cd can be the result of multiple processes, for example the electron conversion decay of ^{111}In. ^{111}In is likewise a widely used PAC probe. Though as this process in 99, 99% of the decay events leads to an excited ^{111m}Cd isomeric state with an energy of $E = 416.63$keV, the excited states with our desired energy of $E_i = 396$keV have to be produced in another way.[49] The direct reception of ^{111m}Cd nuclei is possible online at ISOLDE though the proton bombardement of a molten Sn target which is heated up to 2300K. The great advantage of ^{111m}Cd is the omission of the element transmutation during the decay.[50] It is also possible to produce ^{111m}Cd by irradiating metallic Cd pieces in a neutron flow at the reactor. However, there is no reactor with such an implanter facility, so the ^{111m}Cd ions have to be diffused in the samples (radiochemistry after dissolving the activated Cd piece into a solution). In summary, implantation of ^{111m}Cd is only possible at ISOLDE.

3.3 Ion implantation and PAC measurements

To implant the probe ions in the BFO samples, the sliced pieces were placed on the sampleholder as shown in Figure 3.3(a). To ensure electrical conductivity, double-sided carbon adhesive tape was used to attach the samples. The sampleholder was then mounted on a positioning mechanism, which allows the movement of the sampleholder inside the high vacuum SSP chamber to ensure a well focused ion beam on only one sample position at a time. The produced high purity beam of the radioactive cadmium isomer ^{111m}Cd is focused on the BFO samples with an accelerator voltage of 30keV, reaching implantation depths of around 116Å for an incidence angle of 0° as shown in Figure 3.3(b).

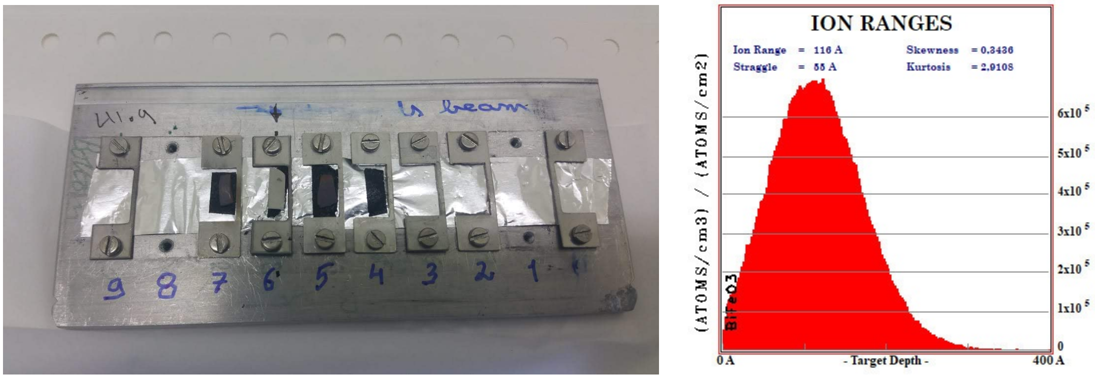

(a) (b)

Figure 3.3: (a) Sample holder with BFO samples on position 7 and 5. (b) Ion depth profile of ^{111m}Cd implanted in BFO with 30keV. Simulations done with the SRIM software package.[51]

Implantations were done at room temperature until an approximate number of 10^{11} atoms per square centimetre sample surface was reached, leading to different implantation durations depending on the ion flux achieved by the target. The now active samples were directly transferred into the fully digital 6-detector spectrometer available in the SSP group laboratory within the ISOLDE facility. The so called DIGIPAC setup, shown in Figure 3.4(a) uses six $LaBr_3$(Ce) scintillators mounted on XP2020URQ photomultipliers in cube arrangement and is able to record the coincidence events of 30 independent detector combinations. The data is directly digitalized, fed to a software program running on a personal computer and the energy spectra as well as the coincidence time histograms are calculated.[52]

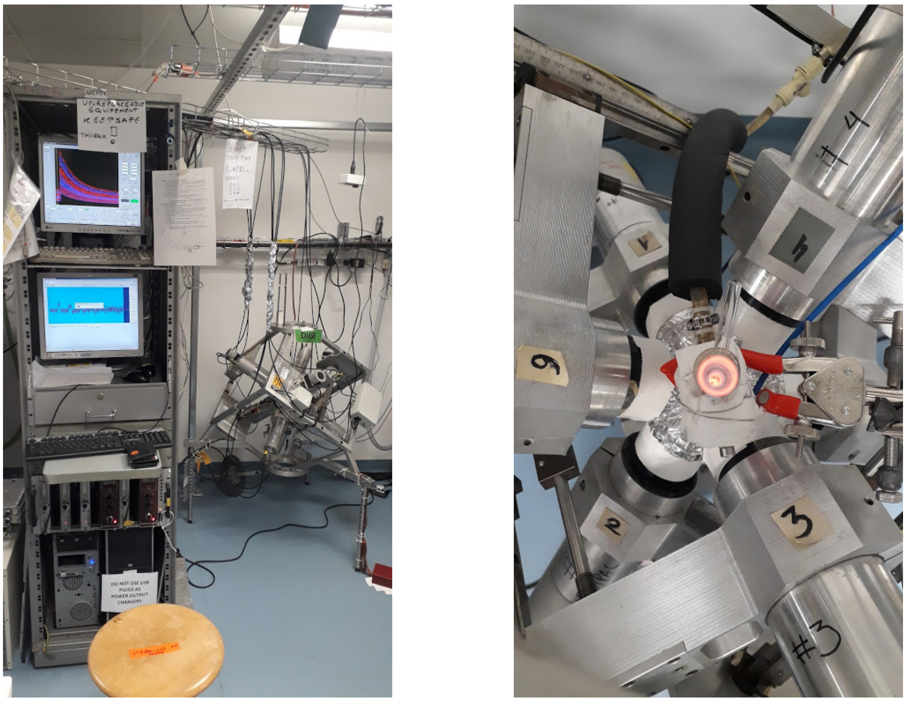
(a) (b)

Figure 3.4: (a) The DIGIPAC setup: The detector cube with the furnace in its center to the right and the digitalisation and computing tower to the left. (b) View of the furnace in the center of the detectors during a measurement at high temperature (thermal radiation visible)

With the water cooled furnace placed in the center of the detectors, depicted in Figure 3.4(b), high temperature measurements up to 850°C were performed. Therefore, the furnace was supplied with two Delta Elektronika SM7020 power supplies. Temperature controlling was done manually through voltage adjustments in order to stabilize the temperature signal given by a NiCr-Ni thermoelement which is directly placed inside the furnace. All measurements were performed under air atmosphere and without prior annealing.

3.4 XRD Measurements

The powder diffractograms were performed in air using a PANalytical X'Pert Pro MPD θ-θ diffractometer equipped with an Anton Paar HTK 1200 high temperature chamber and an X'celerator 128 channel detector. All XRD measurements were conducted at the X-Ray center of the Vienna University of Technology in Vienna, Austria. For temperature point measurements, intensity data were collected in the 2θ=20°-70° range with a scan length of 2.122° with 55,2 s exposure per scan length resulting in overall measurement times of about 45 minutes. Data were converted into step size bins of $0,0084°$. Every step was measured for 55,2 seconds leading to an overall measurement time of about 45 minutes due to the line detector with 128 channels. This measurement routine was used to determine the samples overall phase composition at different temperature points around the presumed Curie temperature, suggested by the PAC measurements. Sweep measurements covering the area between 30° and 35° as well as between 38° and 45° were performed to determine the exact phase transition temperature. Samples were ground and the powder was placed on platinum sample holders to avoid reactions with typical sample holders like monocrystalline silicon.

4 Results and Comparison

4.1 Simulation Results

As mentioned before, conflicting information on the alpha-beta phase transition temperature has been published by various groups. Since earlier PAC measurements of our group from beamtimes in August and October 2017 as well as April 2018 showed interesting results in the region of the expected transition temperature, a closer investigation of the phase transition suggested itself. The crystal structure of the perovskite BFO offers two different sites for the implanted ^{111m}Cd probe atom, namely the A-site, substituting the bismuth position and the B-site, subsituting iron. To determine the most favourable substitution site as well as to set benchmarks for verification of the PAC results, density functional theory (DFT) simulations were done at University of Aveiro, Portugal, using the Vienna Ab Initio Simulation Package (VASP)[53] program, which supports modelling of atomic and electronic structures of matter. The used calculation technique was the projector augmented wave method with a general gradient approximation.[54] The electric field gradient V_{ZZ}, the anisotropy parameter η and the formation energy ΔH were simulated for Cadmium substituting the Bi-, as well as the Fe site. We calculate formation energies for both cases according to the formula $\Delta H = E_{imp} - E_{pure} - \mu_{Cd} + \mu_{Fe/Bi}$ whereE_{imp} is the energy of the supercell with Cd impurity, E_{pure} is the energy of an equivalent supercell of pure BFO, and μ_{Cd}, μ_{Fe} and μ_{Bi} are the energies (per atom) of the elemental solids hcp-Cd, rhombohedral Bi, and ferromagnetic bcc-Fe. According to this estimation, in α-BFO the energy is lower for Cd substitution at the Bi site in FM (AFM) configurations with respect to substitution at the Fe site, making it the likeliest place of substitution. The quadrupole interaction frequency ω_0 was then calculated with the use of formulas 2.7 and 2.12 with the simulated values of V_{ZZ}, η and $Q = 0,641(25)$barn[55]. Even though BFO is paramagnetic at our measurement temperatures, the paramagnetic order is very difficult to simulate. As a workaround, all simulations were done for ferromagnetic (FM) and G-type antiferromagnetic (AFM) magnetic spin order to determine the EFGs dependence on magnetic ordering in general. Simulation results and the calculated values of ω_0 of the α-phase, the β-phase and an additional ternary phase, $Bi_2Fe_4O_9$ which will be detailed in section 4.2.4, can be found in table 4.1.

System		$V_{zz}^{DFT}[\frac{10^{21}V}{m^2}]$	η^{DFT}	ΔH^{DFT} [eV]	ω_0^{DFT} [Mrad/s]
α-BFO (FM / AFM)	Cd @ Bi	5.72 / 5.37	0/0	8.4 / 2.6	80.3-86.8 / 75.4-81.5
	Cd @ Fe	5.46 / 4.07	0/0	8.8 / 5.5	76.7-82.9 / 57.1-61.8
β-BFO (FM / AFM)	Cd @ Bi	-7.51 / -6.88	0.39 / 0.26	4.2 / 1	105.4 - 113.97 / 96.57 - 104.41
	Cd @ Fe	2.37 / 8.43	0.87 / 0.18	-	33.3 - 35.9 / 118.33 - 127.93
$Bi_2Fe_4O_9$ (FM)	Cd @ Bi	9.99	0.12	-	140.22 - 151.61
	Cd @ Fe	7.99	0.84	-	112.15 - 121.25

Table 4.1: Simulated values of V_{zz} and ΔH as well as the calculated value of ω_0. The range of the results of ω_0 is caused by the uncertainity of Q.

As the results of the α-phase show, the formation energy ΔH is lower in both the FM and the AFM order in the simulated system of Cadmium substituting the A-site. Thus a Cd substitution on the bismuth site is considered to be energetically more favourable than a substitution on the iron site, which is backed by the findings of Gebhardt et al.[56].

4.2 Experimental Results

4.2.1 PAC Results

Figure 4.1 shows the experimental R(t) functions as well as Fast Fourier Transformation (FFT) data with fits of the measured BFO samples at measurement temperatures between 800°C and 850°C. The FFT analysis is a helpful tool to visualize the R(t) function through the transition frequencies ω_n and their ratio. The connection to the asymmetry parameter η (see Figure 2.1) of the containing EFGs is directly visible. As mentioned in Sections 4.1 and 4.2.2, the Cd probe ion substitutes the Bi site within the BFO sample material, leading to sensitivity to changes in its nearest surrounding, which is set up by oxygen atoms forming coordination polyhedra around the Bi(Cd) atom. The change from a sixfold coordination in the α-phase to an eightfold coordination in the β-phase results from a change of the Bi-site symmetry. The Bi ion in the α-phase is located on a threefold rotation axis so symmetric by threefold rotation (site symmetry *3*, trigonal point group). On the other hand, the site symmetry of the Bi position in the β-phase is m, which refers to a monoclinic point group, meaning that the Bi ion is located on a mirror reflection plane and so symmetric by mirror reflection. This change in symmetry is accompanied by a change in average coordination lengths from $d_{Bi-O_\alpha} = 2,42Å$ [57] to $d_{Bi-O_\beta} = 2,64Å$ [25], both visible in the PAC results as the following chapter will illustrate.

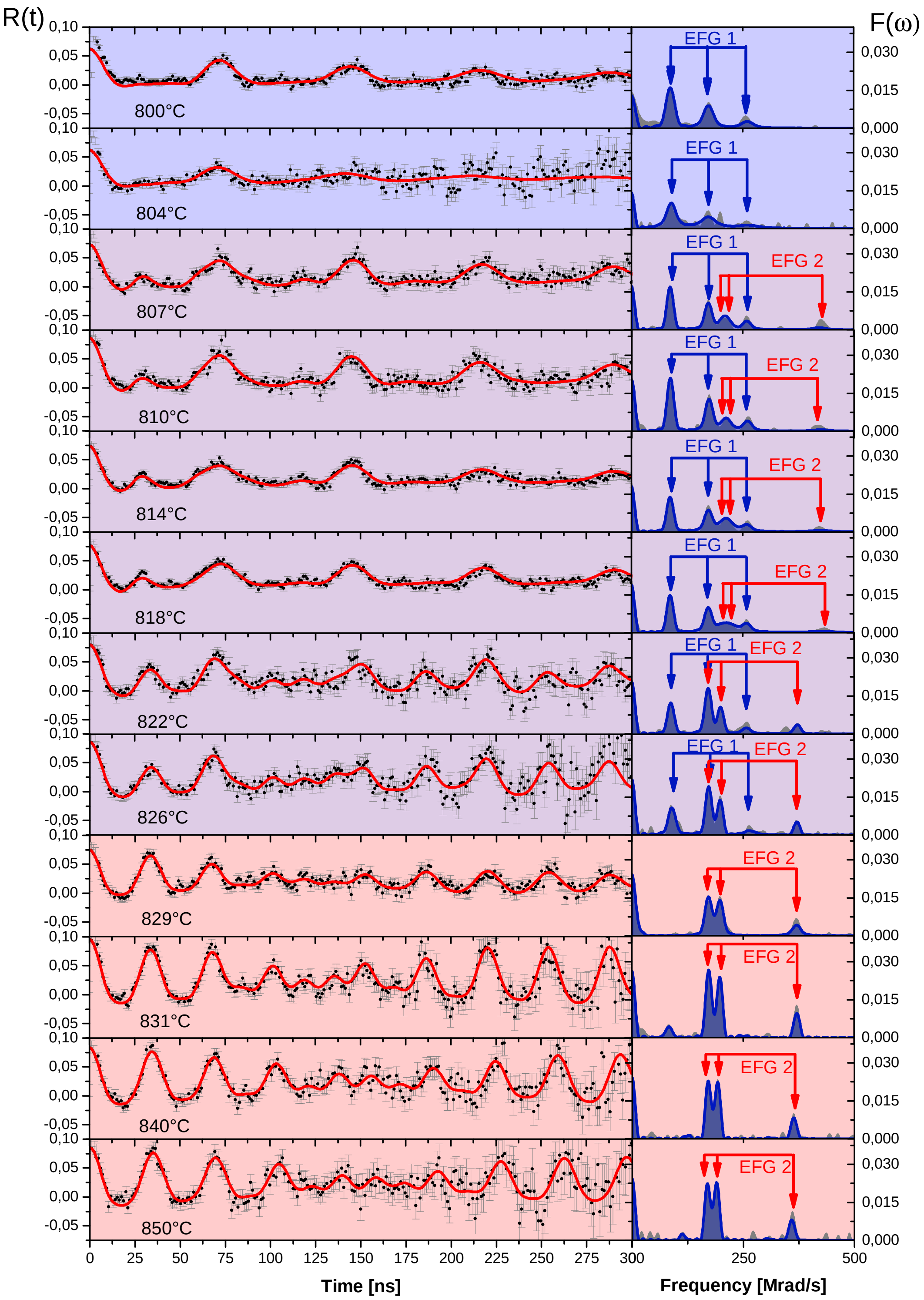

Figure 4.1: TDPAC spectra with fitting functions in red and FFT showing the measured EFGs

The visualization of the single EFGs in Figure 4.1 already hints towards the changes happening during the phase transition from the *R3c* to the *Pbnm* phase as it shows a clear assignment of EFG1 to the α-phase and of EFG2 to the β-phase. Clearly, the EFGs show differences in their strength, visible through the quadrupole interaction frequency (compare to Equation 2.7) and their symmetry (EFG1 is symmetric, EFG2 is highly unsymmetric), visible by the transition frequencies ratio as mentioned before. The data acquisition as well as the fitting and the calculation of the experimental EFG were performed with the GFIT19 software package, a modified version of the NNFit software package[41, 58]. Hyperfine parameters of all fits were calculated and can be found in Table 4.2.

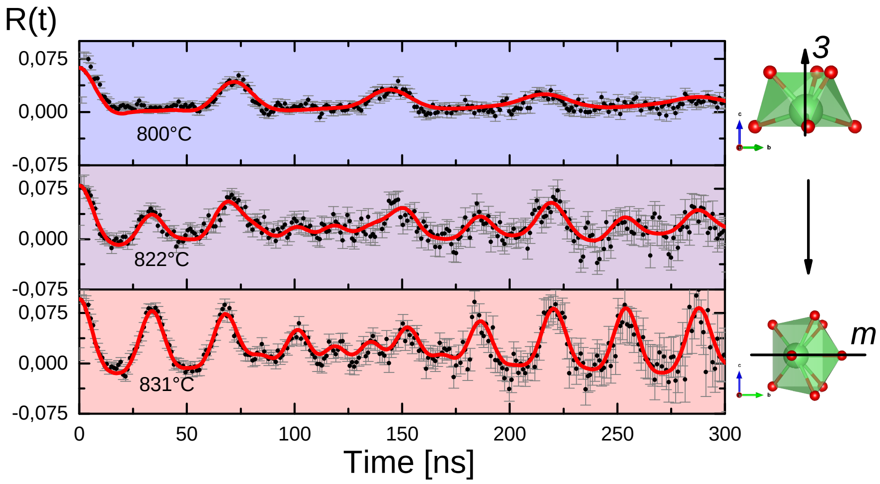

Figure 4.2: Three distinctive PAC spectra showing single α-phase on top, the disordered range with a combination of α and β coordination in the middle and pure β-phase in the bottom spectrum with specific Bi(Cd)-O polyhedra with symmetry elements to the right.

The higher number of coordinating oxygen atoms in the surrounding of the Cd probe atom in eight-fold coordination (β-phase) causes an increased quadrupole interaction frequency with respect to the six-fold coordination in the α-phase as can be seen in Figure 4.2. Up to a measurement temperature of 804°C, only the lower frequency EFG ($\omega_0 \sim 86$ Mrad/s) is present. Compared with the simulation results listed in Table 4.1, we associate this field gradient (EFG1) to α-BFO in ferromagnetic order with Cd@Bi. The measured asymmetry parameter η matches the simulated value reasonably well. As is visible on the FFT of EFG1 in Figure 4.1, the low value of η close to zero leads to a $\omega_1 : \omega_2 : \omega_3$ ratio of $1 : 2 : 3$ (compare to Figure 2.1). Starting at 807°C, also the high-frequency field gradient ($\omega_0 \approx$ 100-120 Mrad/s) appears. This EFG is linked to β-BFO in ferromagnetic order (compare with Table 4.1), also with Cd@Bi. The mismatch of the measured and the simulated value of η is considered less important than the matching values of $\omega_0(V_{zz})$[59]. Above 826°C, only the high-frequency field gradient (EFG2, β-phase) is detected.

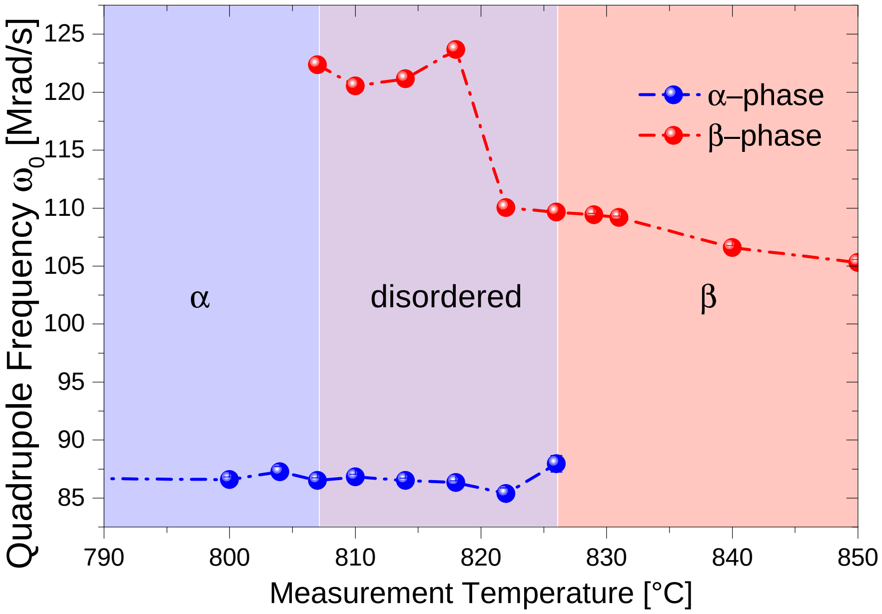

Figure 4.3: Temperature dependence of the quadrupole interaction frequency ω_0. The blue area shows the rhombohedral α-phase region and the red area the orthorhombic β-phase region with the area of disordered coordination in purple in between. If no errorbars are visible, the symmetrical error is smaller than the marker size.

	α-phase				β-phase			
Temp. [°C]	ω_0^{PAC} [Mrad/s]	η^{PAC} [1]	δ^{PAC} [%]	%	ω_0^{PAC} [Mrad/s]	η^{PAC} [1]	δ^{PAC} [%]	%
500	106.43(5.63)	0.44(7)	30.32(6.66)	100				
603	91.31(2.95)	0.43(6)	19.03(2.46)	100				
650	88.5(27)	0.14(2)	4.64(38)	100				
703	86.79(1.08)	0.23(3)	9.85(1.49)	100				
776	86.77(52)	0.16(2)	9.98(71)	100				
800	86.58(25)	0.103(19)	5.30(33)	100				
804	87.27(46)	0.16(4)	10.28(58)	100				
807	86.52(22)	0.075(9)	2.03(27)	78.14(5.26)	122(0)	0.919(7)	0.15(72)	21.86(2.35)
810	86.81(23)	0.022(17)	2.60(27)	78.66(9.35)	120.54(0)	0.997(37)	4.14(1.24)	21.33(2.53)
814	86.52(21)	0.07(2)	3.27(26)	64.85(6.38)	121.14(0)	0.996(16)	5.64(74)	35.15(2.39)
818	86.34(15)	0.083(15)	2.23(18)	60.67(2.08)	123.67(0)	0.928(33)	9.76(1.24)	39.32(2.28)
822	85.39(47)	0.158(1)	2.54(59)	50.20(5.69)	110.05(0)	0.828(4)	0.68(27)	49.80(5.63)
826	87.96(72)	0.151(22)	4.41(94)	48.95(4.94)	109.66(0)	0.832(5)	0.026(58)	51.04(5.21)
829					109.43(12)	0.832(4)	2.19(19)	100
831					109.18(14)	0.842(3)	0.21(13)	100
840					106.6(18)	0.861(4)	0.61(17)	100
850					105.32(25)	0.865(5)	0.52(23)	100

Table 4.2: Experimental PAC values of hyperfine parameters

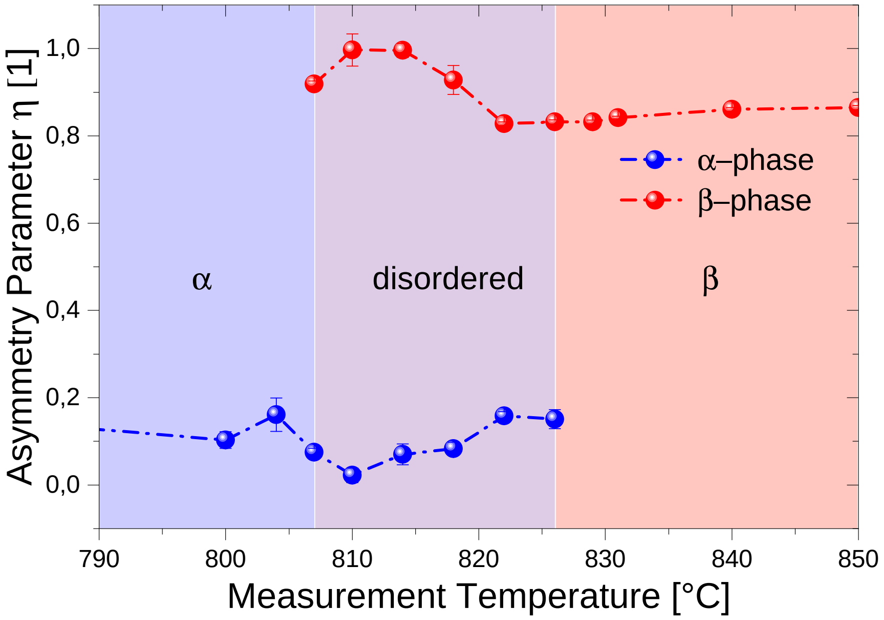

Figure 4.4: Temperature dependence of the asymmetry parameter η. The blue area shows the rhombohedral α-phase region and the red area the orthorhombic β-phase region with the area of disordered coordination in purple in between. If no errorbars are visible, the symmetrical error is smaller than the marker size.

As seen in Figure 4.3, the ω_0-values of the α-phase are practically stable throughout the temperature increase. On the other hand, the quadrupole frequency of EFG2 which is assigned to the β-phase shows a decrease from $\omega_0 = 123.67$ Mrad/s at 818°C to $\omega_0 = 110.05$ Mrad/s at 822°C. This can also be seen in the FFT functions in Figure 4.1 as EFG2 clearly changes between 818°C and 822°C. This prominent feature is the indication for the event of the phase transition. The discordant values of ω_0 of EFG2 right before that decrease indicate the following: With increasing temperature and the approaching of the phase transition temperature, local coordination disordering of the Bi-site, which below 820°C is still in its sixfold α-phase coordination, appears. This means that a pseudo m-symmetry coordination, which actually belongs to the not yet existing β-phase, starts to appear on the 3-symmetry site of the Bi ion. This unknown disordered coordination distorts the EFG and leads to the high values of ω_0. The second parameter to distinguish between the α- and the β-phases is the asymmetry parameter η. As clearly seen in Figure 4.4, the α-phase appears in a rather symmetric setting ($\eta_\alpha \sim 0.1$) compared to the β-phase ($\eta_\beta \sim 0.9$). One should note that there is also a slight change of the asymmetry parameter in EFG2 between 814°C and 822°C as the value drops from $\eta_{814} = 0.996$ to $\eta_{822} = 0.828$. This dynamic is linked to the coordination disordering which was described before. The surrounding of the probe atom thus experiences a noticeable structural change in this temperature region. An indication for this dynamic are also the slightly increasing values of damping δ in the β-EFG between 807°C and 818°C (Figure 4.5), as with the increasing number of disordered Bi-coordination sites the EFG distribution width broadens. A nearly linear decrease of the quadrupole interaction frequency of the β-EFG is visible in Figure 4.3 starting from 822°C. This behaviour can be linked to the temperature expansion of the unit cell, which is also seen in the XRD results in Figure 4.8. The damping δ, shown in Figure 4.5, is generally low at all measurements, indicating a rather narrow EFG distribution and thus allows an accurate analysis. It also shows that the change in EFG due to fluctuations is low. Thus, the crystal structure itself changes likely due to longer range interactions. The disordering of the Bi-sites and the following changes in coordination are an independent effect, which are only visible locally. The visible changes in damping δ, even though they are small, have a significant meaning. EFG1 by comparison shows a peak in damping at the 804°C temperature point. This feature indicates

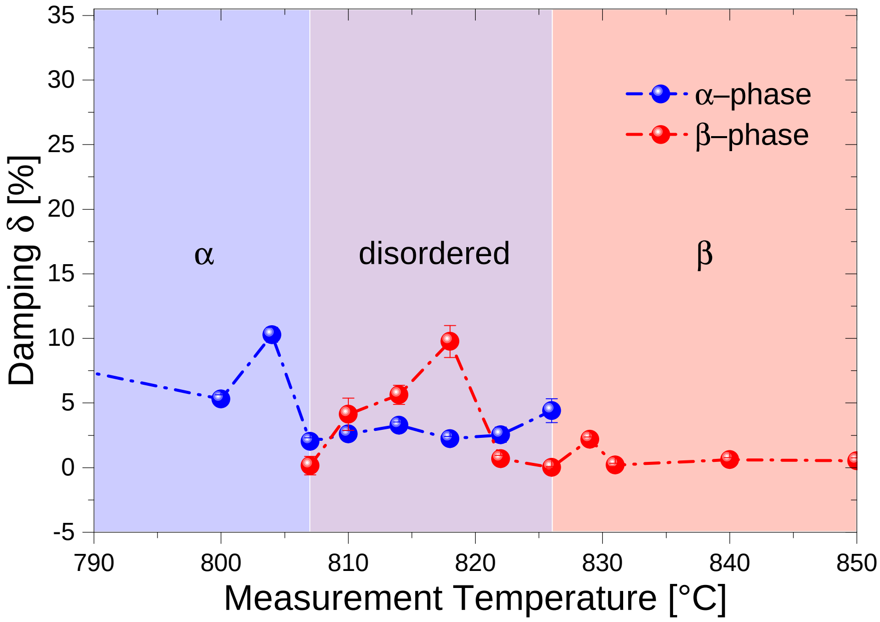

Figure 4.5: Temperature dependence of the damping parameter δ. The blue area shows the rhombohedral α-phase region and the red area the orthorhombic β-phase region with the area of disordered coordination in purple in between. If no errorbars are visible, the symmetrical error is smaller than the marker size.

the emergence of the β-phase EFG, caused by the mentioned pseudo m-symmetry coordinations, which is already present at the next measurement point at 807°C. The increasing δ-value between 807°C and 818°C in EFG2 was already addressed before. At 822°C, the damping again drops to a value of $\delta_{822°C} = 0,68(27)\%$. This indicates that the phase transition is completed. From now on the Bi ion sits on the mentioned site with m-symmetry in an eightfold coordination. EFG1 exists up to a temperature of 826°C, where the last remaining pseudo coordinations with 3-symmetry vanish. As can be seen in Figure 4.6, the fraction of EFG2 is increasing with increasing temperature while the fraction of EFG1 decreases. This, once again, underlines the dynamic of the coordination change as the ^{111m}Cd probe ion forecasts the phase transition.

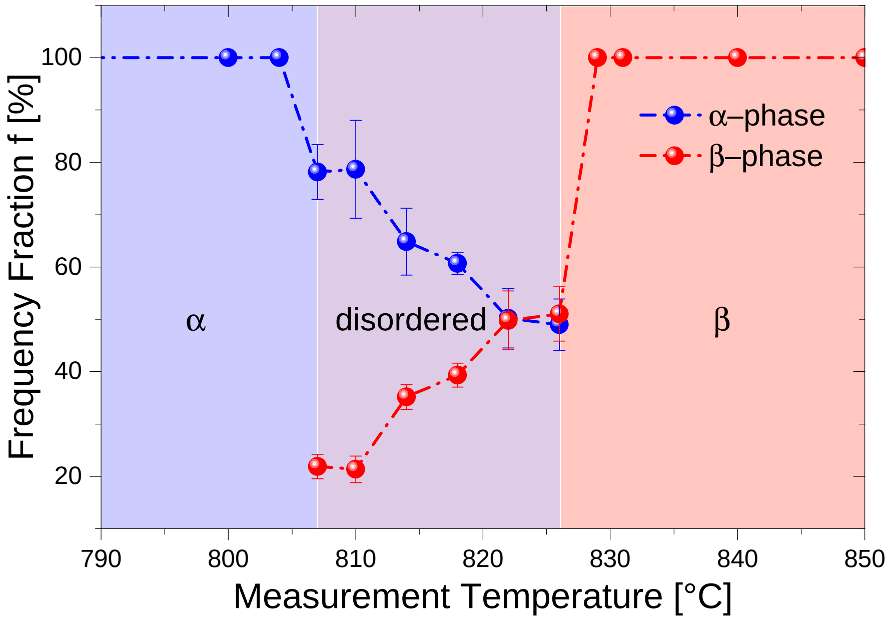

Figure 4.6: Temperature dependence of the frequency fraction f. The blue area shows the rhombohedral α-phase region and the red area the orthorhombic β-phase region with the area of disordered coordination in purple in between. If no errorbars are visible, the symmetrical error is smaller than the marker size.

4.2.2 Probe site assignment

Site assignment for tracer ions is sometimes a difficult tast. Here, we collect arguments for A or B-site substitution. DFT simulations, which are only strictly valid at a temperature of 0K, might to some extent be uncertain at our measurement temperatures. A comparison of the ionic radii of the involved elements strongly suggests a substitution of the Bi site through the Cd ion. Depending on the coordination number (CN), the ionic radii of all ions vary as summarized in Table 4.3. Bi as well as the Fe cations are assumed to be in an six-fold coordination in the α-phase, with their effective ionic radii of 1.02Å and 0.55Å (low spin) / 0.645Å (high spin) respectively, also the value of a six-fold coordination of Cd^{2+} was taken for comparison. The six-fold effective ion radius of Cd with 0.95Å is much closer to the radius of the Bi ion than to the Fe ion, which is the most important indication for the substitution at the A-site[60]. A substitution of the Fe-cation would necessarily lead to a significant distortion of the unit cell, possibly followed by an asymmetry parameter different from zero. A counterargument would be that ferroelectricity in $BiFeO_3$ is mainly due to the lone pair polarization of the Bi ion. Thus, Cd substituting Bi must experience the local effect of changes in polarization in its field gradient. So, the EFG should change also before the curie point itself (α to β phase transition) is reached. Landau theory predicts a moderate change of the order parameter just beneath such a strong first order phase transition.[61] So unlike in second order phase transitions, where a large change in V_{zz} would have to precede the phase transition, the jump in order parameter at the first order phase transition temperature allows for only moderate changes just beneath T_c. Thus, we observe practically no change in V_{zz} beneath the phase transition temperature and assign this to the very limited temperature range we investigate. In this range no change is within the error bar of analysis with a "moderate" change which would be a few percent only as we know from other data on $BiFeO_3$. The ^{111m}Cd probe site substitution was also a point of discussion in rare-earth orthochromite ceramics. Comparisons with ^{111}In(^{111}Cd) PAC measurements done on rare-earth orthoferrites lead to the assumption that in the particular case of $SmCrO_3$ the ^{111m}Cd probe also occupies the A-site.[62] The ^{111}In(^{111}Cd) probe used to examine the rare earth orthoferrites ($RFeO_3$, REO) occupies both sites, leading to a low frequency EFG describing the Fe-occupancy and a high frequency EFG describing the R-occupancy.[63] As seen in Table 4.3, ^{111}In though has a way smaller ionic radius (0.79Å in sixfold coordination) than ^{111m}Cd, which possibly leads to an occupation of both sites. Rearick et al.[63] also mention that the ^{111}In probe primarily substitutes into the rare earth sites in the heavier REOs. Though bismuth is not a rare earth element, an A-site occupation is is more likely as Bi is a heavier element than all the rare earth elements. Further literature affirming the A-site substitution are the works of Bellakki,[64]

CN	Ion				
	Cd^{2+}	Bi^{3+}	Fe^{3+}	In^{3+}	Mn^{3+}
IV	0.84	-	0.49	-	-
V	0.87	0.99	-	-	0.58
VI	0.95	1.02	0.55 (LS) 0.645 (HS)	0.79	0.58 (LS) 0.65 (HS)
VII	1	-	-		
VIII	1.07	1.11	-	0.923	-
XII	1.31	-	-		

Table 4.3: Effective ion radii of Cd^{2+}, Bi^{3+} and Fe^{3+} ions in Å for different coordination numbers CN.[60]

which addresses Cd-doped BFO and Ishaq et al.[65], which treats Cd-Mn doped BFO. Bellakki states that Cd substitutes only the Bi cation. Ishaq et al. describe that Cd substitutes the Bi site whereas Mn substitutes the Fe site. Reconsidering the ionic radii of Cd and Mn (Table 4.3) this is expected as the Mn value is significantly closer to the one of Fe whereas the ionic radius of Cd is similar to the one of Bi. Sato et al. also describe ^{111m}Cd as substituting the R and A-sites in doped perovskite manganese oxides ($R_{1-x}A_xMnO_3$).[66] As in our work only one EFG is assigned to the α-phase, a distinction is more difficult but was still done in favour of the A-site concerning other literature, DFT simulation results as well as based on ionic radii. Also, as the results suggest, the coordination of the probe atom experiences massive changes. As the coordination of the Fe atoms stays rather unchanged, a substitution of Fe by Cd seems very unlikely. In summary, substitution of Bi by ^{111m}Cd on the A-site is what we conclude from these arguments.

4.2.3 XRD Results

Point Measurements

Figure 4.7 shows XRD patterns of BFO, measured at temperatures between 800°C and 830°C as well as XRD patterns calculated from crystallographic information files (CIFs) for α-BFO in $R3c$ and β-BFO in $Pbnm$ setting. The structural data given in the CIF were also used for the simulations described in chapter 4.1. This gives a first impression of the agreement of the results of PAC and XRD measurements. As can be seen in Figure 4.7, the calculated diffractogram for the α-phase coincides perfectly with the measured data up to 814°C, thus this temperature region is considered to represent the single α-phase. Rietveld refinement backs this as the β-phase does not appear below 818°C. This temperature point can be considered as the phase transition point showing behaviour of a first order phase transition, as α and β phase are present. This diffractogram is mostly consistent with the β-phase. However, minor amounts of the α-phase are still observed for example by the not completely vanished 104 reflection at $2\theta = 31.5°$. Rietveld refinement results in a α-BFO mass fraction of ca. 8%. However, this aspect could be the result of an existing temperature gradient within the sample. The additional reflections appearing in the measured diffractograms are either Pt peaks from the sample holder (marked with $*$) or the known decomposition products $Bi_2Fe_4O_9$ (#) and $Bi_{25}FeO_{39}$ ($\sim$) as BFO is metastable at elevated temperatures.[67] The two reflections labelled with x were not identified but could result from sample contamination during the measurements. For clarity, the intensities in this plot were normalized to a value of one, meaning that all values were divided by the highest appearing intensity value of the particular measurement. The relative intensities and their ratio was not changed through this. Another feature to distinguish between the phases is the background color of the plots. The diffractograms with a majority of α-BFO are highlighted blueish, the ones with a majority of β-BFO are highlighted redish. The measurement where both phases are apparent (818°C) is highlighted in purple. This color code is used throughout most data plots in this work.

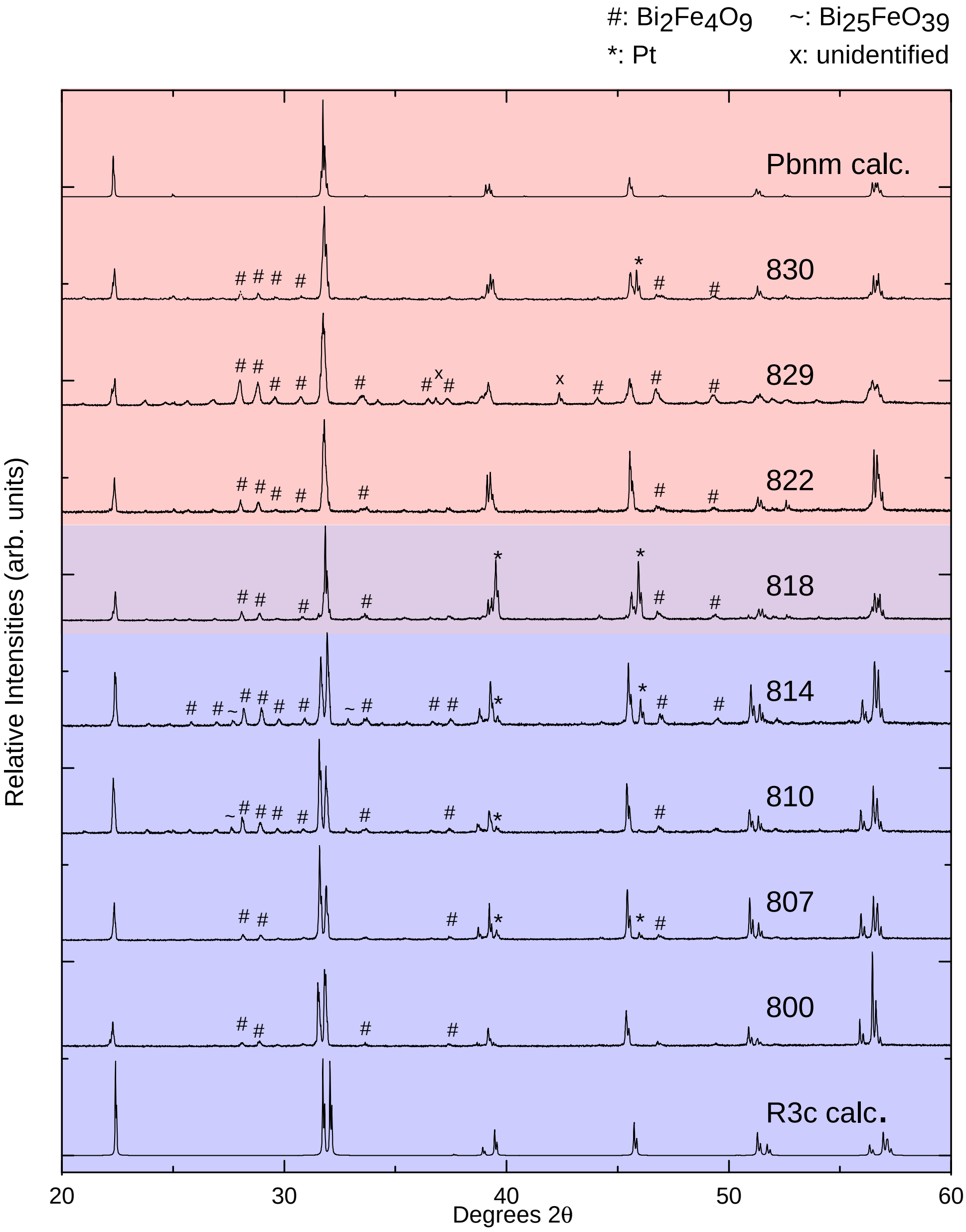

Figure 4.7: Temperature dependence of X-ray diffractograms measured between 20°-70° (graphs are only shown up to 60° as no information gain is achieved from reflections above 60°) at increasing temperatures around the phase transition temperature. The top and bottom graph show calculated diffractograms of BFOs *R*3*c* and *Pbnm* structure respectively.

Results of Rietveld Refinement

To determine the unit cell characteristics, the XRD data were fitted with the Rietveld refinement method. Properties like cell parameters, unit cell volumes, existence of phases and phase fraction were defined. As Figure 4.8 shows, the volume contraction appearing at the phase transition, which was already described in Section 1.4, is clearly visible in our XRD results. In the following two graphs the purple area, indicating the presence of both phases, is missing because coexistence of both phases was only observed for a single temperature point (818°C).

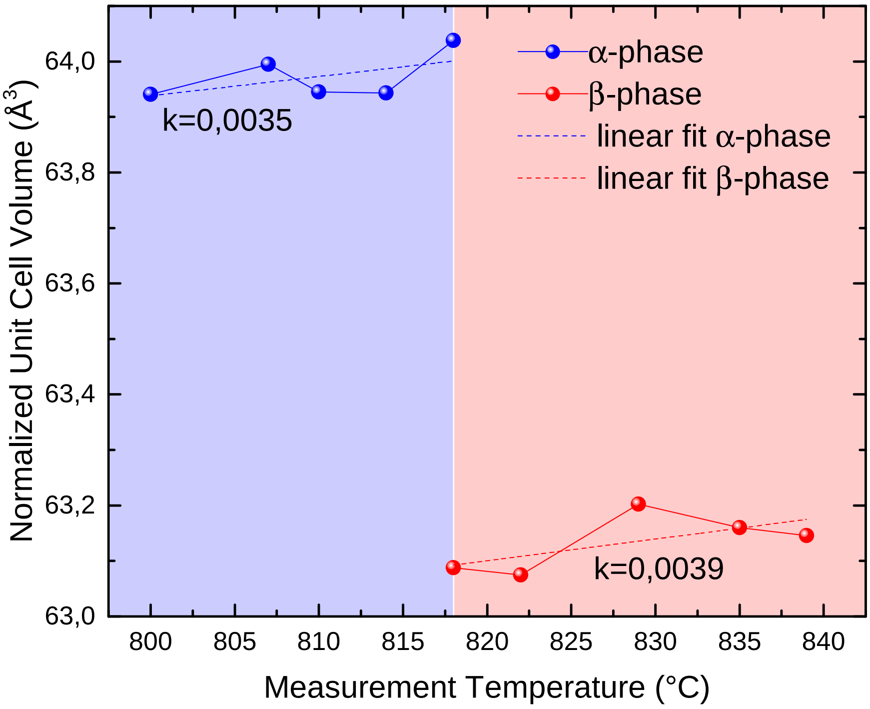

Figure 4.8: Temperature development of the normalized unit cell volume of the α-phase in blue and the β-phase in red. At 818°C the described lattice contraction appears.

The normalized unit cell volume, which is plotted on the ordinate, is the unit cell volume divided by the number of formula units contained in the unit cell. For α-BFO, the unit cell volume is divided by six, for β-BFO it is divided by four. The thermal expansion in both phases is visible in Figure 4.8. The slopes of the linear regressions are quite similar with $k_\alpha = 0,0035\text{Å}^3/\text{K}$ and $k_\beta = 0,0039\text{Å}^3/\text{K}$.

The phases present in the measurements and their temperature evolution can be seen in Figure 4.9. The plot shows the mass fraction of the α-phase and the β-phase, as well as the mass fraction of the ternary phase $Bi_2Fe_4O_9$. The mass fraction of $Bi_{25}FeO_{39}$ was so small, below 1%, so that this fraction was ignored. Possible fractions of Pt, caused by reflections of the sample holder, were not incorporated in the refinement and thus are also not shown in the plot.

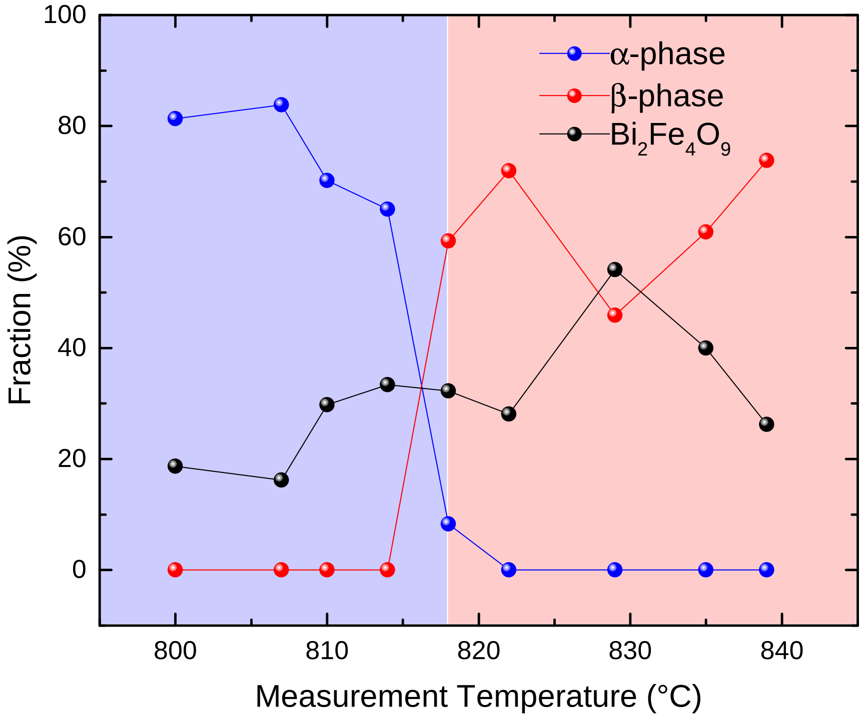

Figure 4.9: Temperature development of the phase fractions of α-BFO in blue, β-BFO in red and $Bi_2Fe_4O_9$ in black. At 818°C both BFO phases are present.

Figure 4.9 shows the refined mass fractions of the XRD patterns visible in Figure 4.7. There are a few features which can be seen in both figures. For example the presence of both phases at the temperature of 818°C as well as the comparably high amount of $Bi_2Fe_4O_9$ at 829°C. A reason for this "peak" of the ternary phase fraction is difficult to find and possibly is an artifact. As the measurement followed the same procedure, heating or measurement time should not make any differences compared to the other measurements. One reason could be a sample of lower quality containing slightly more defects which can work as a catalyst for the formation of ternary phases. A further possibility is the described back reaction to the parent form of BFO above certain temperatures.[68] This phenomenon though is not backed by the results shown in the next Section 4.2.4.

Sweep Measurements

As has been mentioned before, the phase transition was also analysed through sweep measurements in a small angle range to ascertain the exact phase transition temperature. A suitable angular range for this examination was found to be the 104-110 reflection pair of α-BFO at aproximately $2\theta = 31.5°$ and $2\theta = 32°$ respectively, which merges to a narrow peak triplet of *200, 121* and *002* of the orthorhombic β-phase when the structural phase transition occurs. This peak merging can be seen clearly in Figure 4.10.

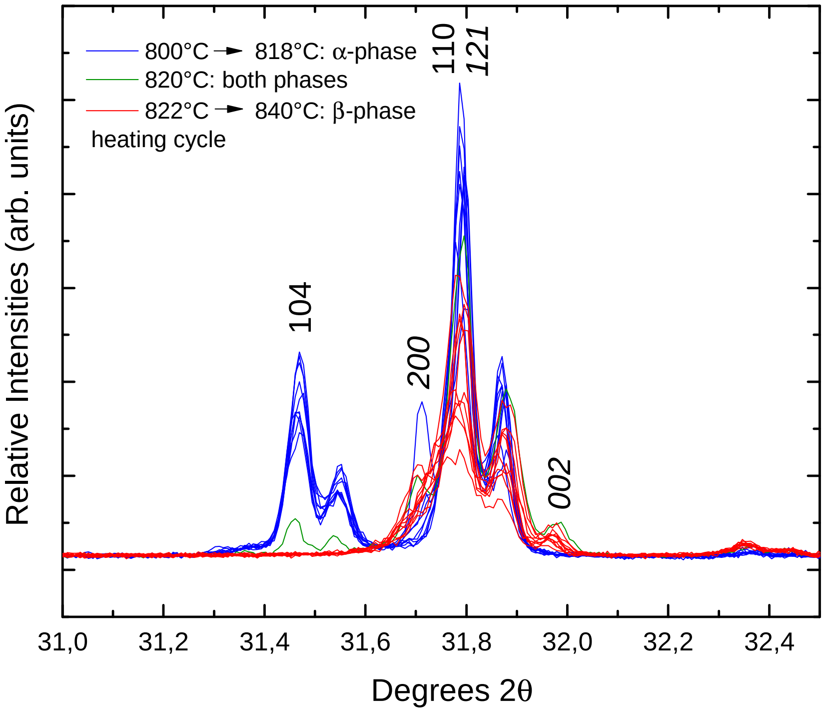

Figure 4.10: Evolutions of reflections with temperature during the heating cycle. α-phase in blue, mixed phase in green and β-phase in red. Reflection description of β peaks are italic.

The sweep was measured with temperature steps of 2K between 800°C and 840°C. Until a temperature of 818°C, the diffractograms show clear evidence of only the α-phase being present. In the 820°C dataset, shown in green, the diffractogram shows a distinctly weaker intensity at the 104 peak and also an attenuated intensity of the 110 peak, leading to the conclusion that the α-phase is vanishing, representing the region of coexistence of both phases. In all datasets acquired above 820°C, all shown in red, only the mentioned triplet (*200,121,002*) of the β-phase is present. The phase transition is mostly visible through the vanishing 104 α-reflection. Although the 110 α-reflection of course also vanishes, the appearing very narrow combination of *200, 121* and *002* reflections of the β-phase at similar scattering angles makes a distinction difficult. The temperature difference of 2K between the phase transition temperature observed in this sweep measurements (820°C) and the measurements covering the angle between 20° and 70° (818°C) can be explained through uncertainties of the temperature measurement in the high temperature chamber.

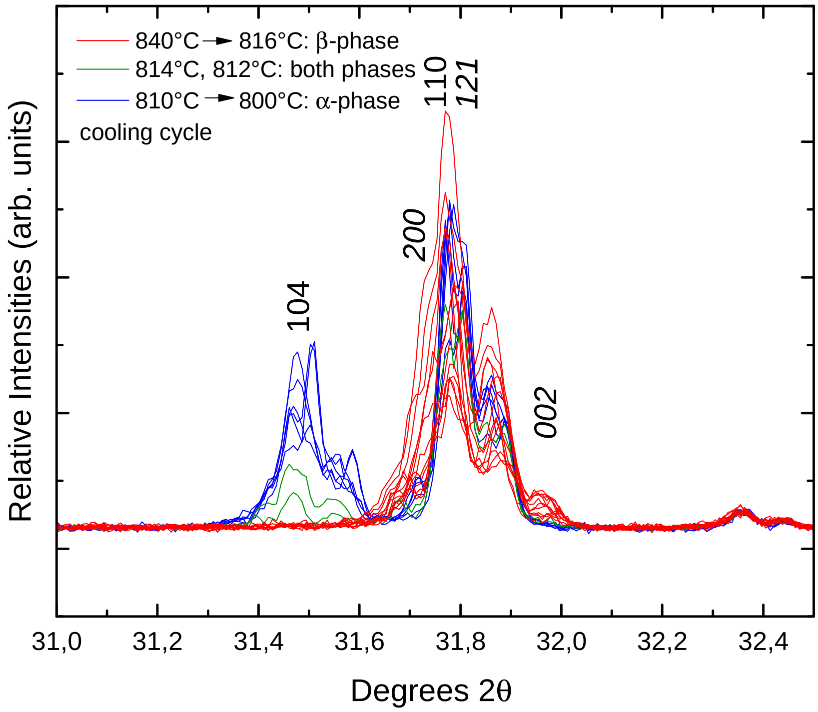

Figure 4.11: Phase transition from the β-phase to the α-phase during the cooling process visible by splitting of the reflection.

The reversibility of the phase change was proven through the same measurement. Directly after reaching $T_{max} = 840°C$ temperature steps of 2K were measured until 800°C were reached again. As Figure 4.11 shows, there is a small hysteresis effect. The phase change during the cooling process starts to appear at 814°C, the fully recovered α-phase is visible at around 820°C. The same reversible phase transition can be seen in Figure 4.12 in the reflection behaviour of two reflections close to $2\theta \sim 39°$. The Figure impressively demonstrates how the 006 reflection of the α-phase disappears when the phase transition temperature of 822°C is reached. The 202 α-reflection is substituted by the *220* β-reflection and the *022* β-reflection appears, close to the K_{α_2}-shoulder of the 202 α-peak.

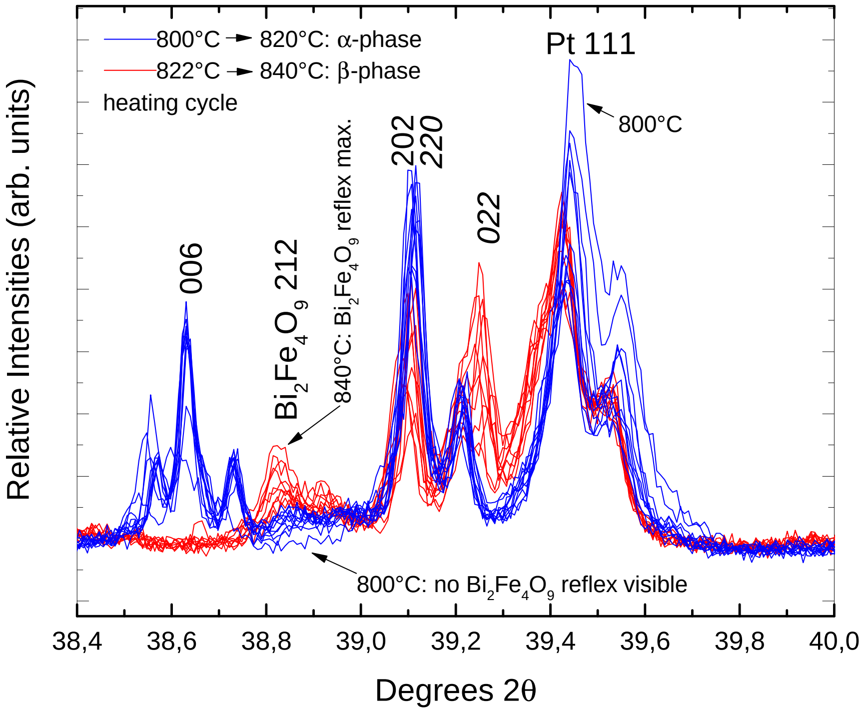

Figure 4.12: Reflection behaviour between 38, 4° and 40° during the heating cycle.

The reflection on the far right of the diagram is the 111 reflection of platinum, the sample holder material. In this peak, the temperature shift of reflections is visible as the peak maximum moves to smaller 2θ angles with increasing temperature caused by lattice expansion. Another feature visible in Figure 4.12 is the emerging of the 212 reflection of the $Bi_2Fe_4O_9$ decomposition phase, addressed closer in section 4.2.4. The peak intensity increases with increasing temperature, starting with no peak at 800°C to its maximum at 840°C. The reflection behaviour during the cooling cycle is shown in Figure 4.13. As expected, it features the same behaviour only in opposite direction. The 006 α-reflection arises at a temperature of 816°C while the *022*-reflection of the β-phase vanishes at exactly this temperature. The singular blue curve which seems to be part of the red *022* peak in Figure 4.13 belongs to the measurement at 814°C, thus already to the α-phase. As opposed to its appearance, this is the K_{α_2} shoulder of the 202 reflection. Apparently, the measurement at 814°C showed noticeably higher intensities than the rest which let this sholder appear as a single peak. The 814°C measurement is denoted in Figure 4.13. The Pt 111 peak again is very distinctive, making it clear that the BFO experiences heavy changes in the measurements temperature range while the position of the platinum reflection is very constant. Another visible feature is the existing 212 reflection of $Bi_2Fe_4O_9$ which is permanently present after the phase developed during the heating cycle (Figure 4.12).

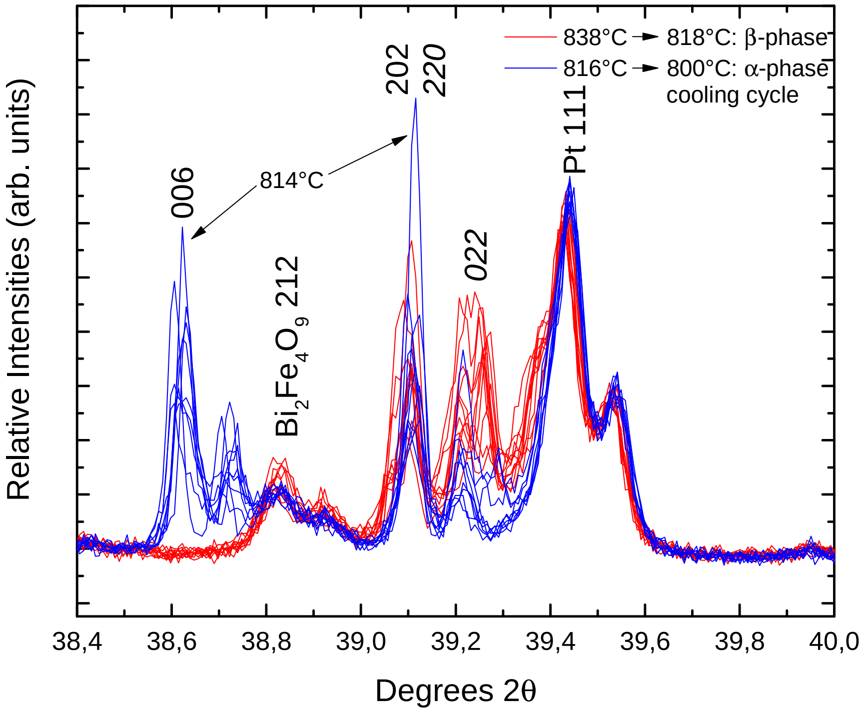

Figure 4.13: Reflection behaviour between $38,4^\circ$ and 40° during the cooling cycle.

4.2.4 Ternary phases $Bi_2Fe_4O_9$ and $Bi_{25}FeO_{39}$

As shown in Figure 4.7, reflections of the ternary mullite $Bi_2Fe_4O_9$ and the selenite $Bi_{25}FeO_{39}$ phases are visible in all measured diffractograms. These decomposition products, which also form under vacuum and inert gas, were not present in the samples before they were subjected to the measurements at high temperatures.

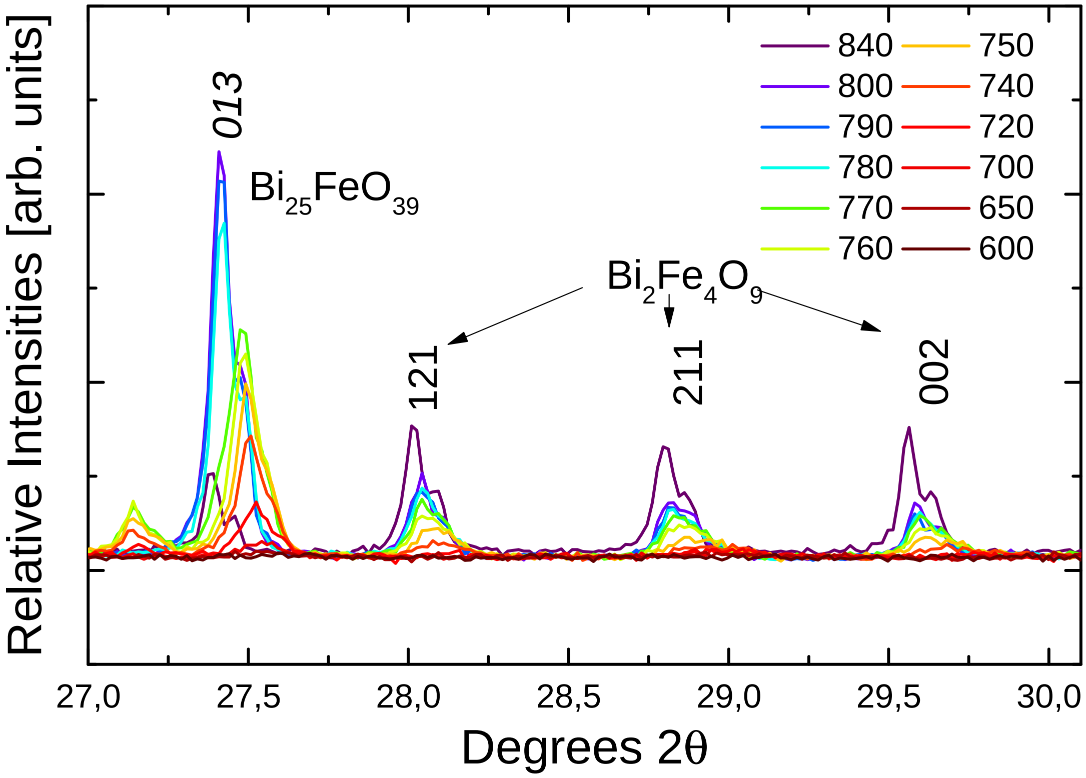

Figure 4.14: Peak growth of ternary phases $Bi_{25}FeO_{39}$ (italic) and $Bi_2Fe_4O_9$ with temperature. The color corresponds to the measurement temperatures as shown in the legend.

In fact, comparisons of diffractograms shown in Figure 4.14 recorded at temperatures between 600C and 800°C show that the impurity phases start to appear at about 650°C with $Bi_{25}FeO_{39}$ already being present at about 650°C, whereas $Bi_2Fe_4O_9$ appears slightly later around 700-720°C. Obviously, these secondary phases are more stable with respect to pure BFO in this temperature range.[68] BFO decomposes into the mullite and selenite phases following the formula $49BiFeO_3 \rightleftarrows 12Bi_2Fe_4O_9 + Bi_{25}FeO_{39}$, leading to significantly higher amounts of the mullite component, which is supported by our Rietveld refinement.[69] Apart from the measurement temperature and time, also the purity of the samples has a big impact on the formation rate of the ternary phases.[70] This might be an explanation for the varying amounts of ternary phase products in our measurements, as diffractograms of samples with high amounts of mullite and selenite phases after the measurement showed already some minor, unidentified peaks before the high temperature measurements. As the maximum measured temperature in our research was 840°C, a halting of the decomposition processes as well as the reverse reaction from the secondary phases back to $BiFeO_3$ as observed by Selbach et al.[68] could not be confirmed. However, Figure 4.14 shows that at 840°C the 013 reflection of $Bi_{25}FeO_{39}$ is significantly weaker compared to the peak intensities at lower temperatures, indicating the beginning of a reduction of this components presence. On the other hand, all peaks of $Bi_2Fe_4O_9$ show stronger intensities even at 840°C. Thus, the thermodynamic stabilities of the two ternary phases might not be equal. The simulation results listed in Table 4.1 were done in order to try a fitting of the PAC results including phase fractions of $Bi_2Fe_4O_9$ with the calculated parameters. However, no phase fractions of the mullite phase were present in the PAC spectra. The appearance of the ternary phases in the XRD measurements, which were conducted after the PAC measurements, could be explained through the second heating process at the XRD measurements which leads to an increase of fractions of those phases. Visible ternary phase fractions in samples which were not exposed to a prior PAC measurement might be caused by the significantly larger surface area of powdered samples in comparison to bulk samples, increasing the volatility of Bi and thus the formation of the decomposition products.

4.2.5 Difficulies encountered during XRD measurements

Si 771 sampleholder

The first, preliminary XRD measurements with BFO were conducted with a standard Si single crystal sample holder, which was cut parallel to the (711) plane to avoid sample holder reflections.

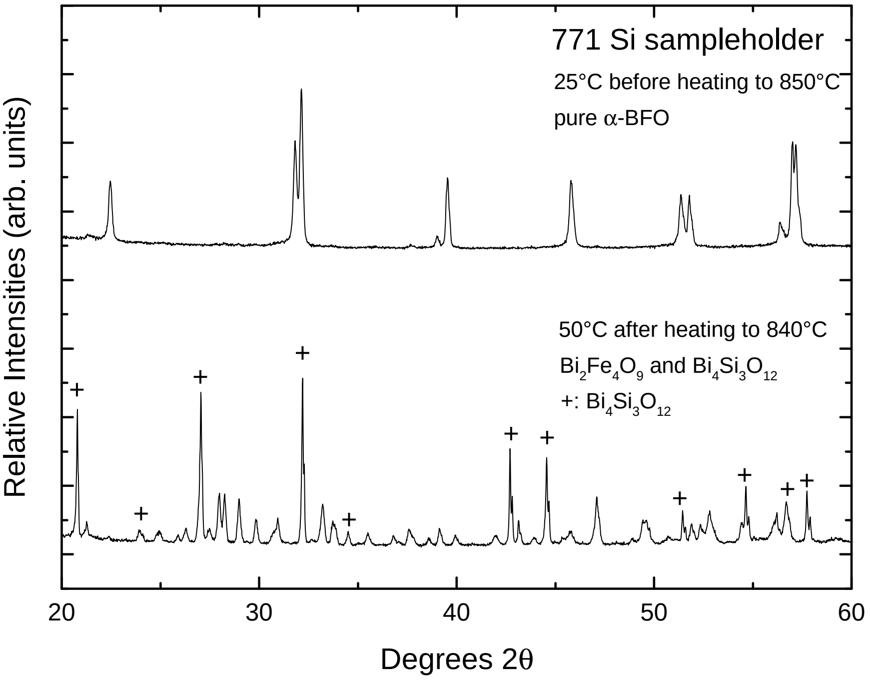

Figure 4.15: Diffractograms of bulk BFO on a 771 Si sampleholder. Top plot measured at RT before heating, bottom plot at 50°C after heating.

Being unaware of the reactivity of BFO with Si compounds, the results were surprising. As Figure 4.15 shows, the pre heating room temperature measurement and the post heating 50°C measurement are fundamentally different although the diffractograms should be similar apart from possible reflections of emerging decomposition products. The diffractograms though show that the original α-BFO phase is not present anymore. The resulting diffractogram shows a mixture of the mullite phase $Bi_2Fe_4O_9$ and the silicate $Bi_4Si_3O_{12}$.[71] Obviously Si reacts with BFO yielding Bi-silicates and leaving behind the Bi-poor $Bi_2Fe_4O_9$, which is also formed as decomposition product when no Si is involved.

Figure 4.16: Picture of the reacted sample holder and the destroyed sample after the measurement. Obviously a melting process took place.

Figure 4.16 shows the 771 Si sample holder with the sample after the measurement. As can be seen, a melting process occurred, destroying the sample holder as well as the sample. This first measurement was done with a bulk sample.

Fused silica (quartz glass) sampleholder

The fused silica sampleholder was tried after successful powder XRD measurements in an attempt to get rid of the additional Pt peaks of the platinum sample holder.

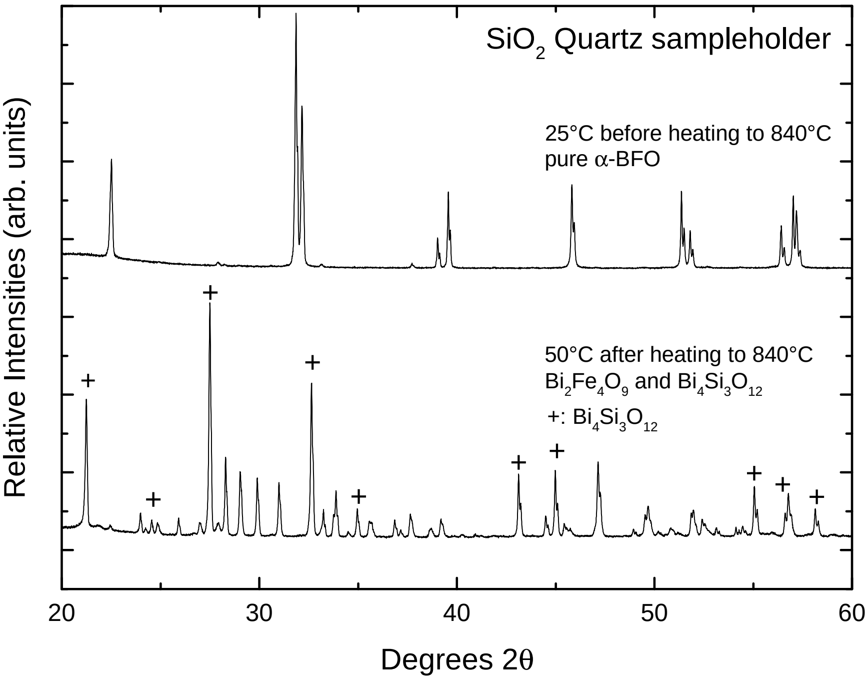

Figure 4.17: Diffractograms of powdered BFO on a quartz glass sampleholder. Top plot measured at RT before heating, bottom plot at 50°C after heating.

As the PAC measurements were all conducted in a quartz glass sampleholder and no reaction was observed, neither macroscopically nor in the experimental results, the expectations were that no reaction will take place between the now powdered sample and the sampleholder. One could expect that the oxophilic Si is less reactive in SiO_2 form than the element. However, also in this case an analoguous reaction to the one with the Si single crystal was observed. The diffractogram in Figure 4.17 shows that the post heating sample done at 50°C also mainly is composed of $Bi_2Fe_4O_9$ and $Bi_4Si_3O_{12}$.

SiN sampleholder

A last attempt to find a sampleholder without Pt reflections was performed using a plate of silicon nitride SiN.

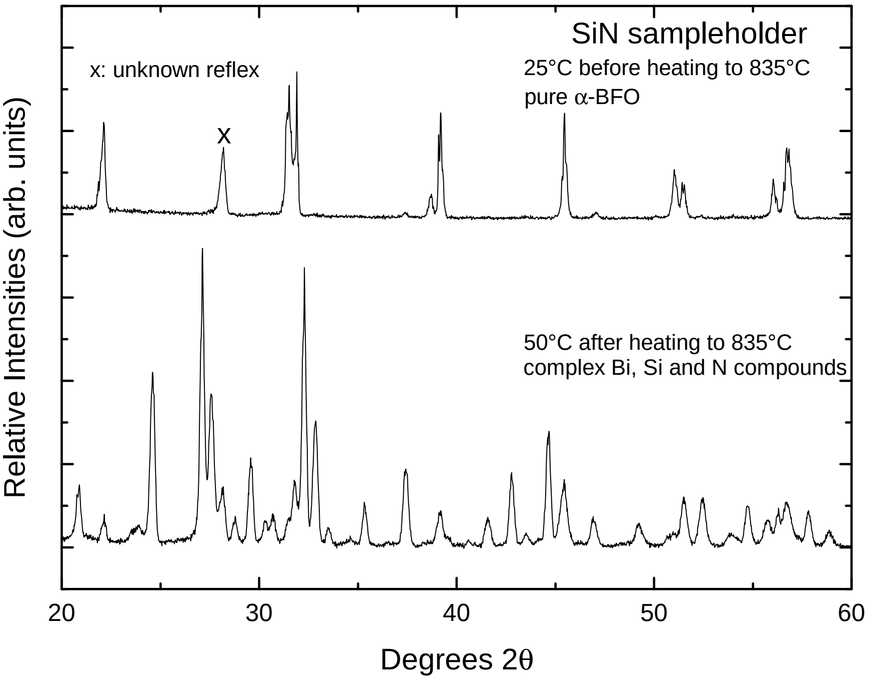

Figure 4.18: Diffractograms of powdered BFO on a SiN sampleholder. Top plot measured at RT before heating, bottom plot at 50°C after heating.

As SiN shows good high temperature stability and a high melting point of about 1900°C, the measurement was expected to proceed without reactions. However, here again the sample showed a reaction with the sampleholder leading to complex Bi-Si-N compunds seen in Figure 4.18. Thus, ultimately the disadvantage of measuring with a Pt sampleholder was accepted. The advantage of Pt, its inertness, was considered to be more important than the possible appearance of its reflections in the XRD patterns, especially because there were only 2 Pt reflections (111 and 200) within the scattering angle range, thus they were well known. The disadvantage was that these reflections are very close to crucial reflections that were used to characterize the phase transition. If the Pt reflections were too high in intensity, they overshadowed the reflections of interest of BFO. Platinum peaks are visible in Figure 4.7, marked with a $*$.

Measurements on bulk samples

A further measurement was attempted with bulk samples in order to not have any Pt reflections in the diffractograms. The idea was that the 1,3mm thick samples would absorb all the x-rays before these reach the the platinum sample holder. Also the Pt sample holder this time was realized smaller than the sample itself, thus it rather acted like a distance holder. This was done to ensure that no Pt was visible, all covered by the BFO sample.

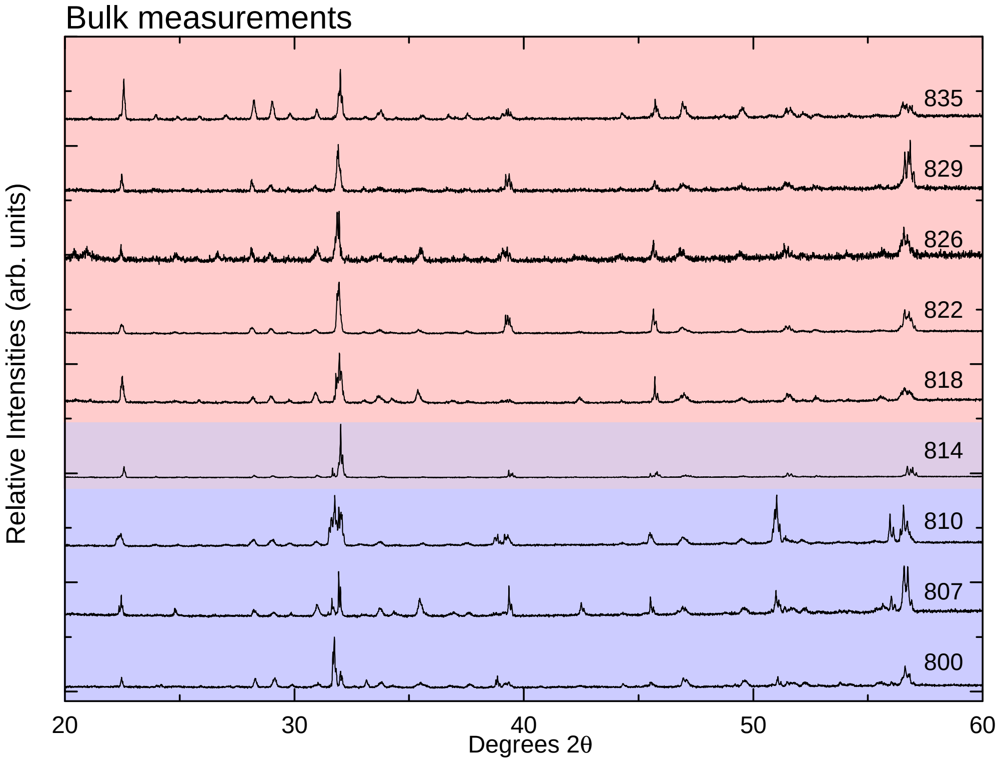

Figure 4.19: Temperature dependence of X-ray diffractograms measured on bulk BFO samples between 20°-70° (graphs are only shown up to 60° as no information gain is achieved from reflections above 60°) at increasing temperatures around the phase transition temperature.

Figure 4.19 shows the normalized diffractograms of the bulk measurements. As can be seen, many of the patterns show bad statistics and thus were difficult to refine with the Rietveld method. A reason for this is the geometry of the Bragg-Brentano method, used for the XRD analysis. Its advantage, the irradiation of constant volumes caused by the widening of the beam at lower measurement angles, became a disadvantage because of the limited size of our samples. Indeed, there are no Pt peaks visible in the XRD patterns done with the bulk samples. However, the powder sample measurements were much better in terms of statistics and the count rates were way higher, which led to the decision to use them for the Rietveld refinement.

5 Conclusion and Outlook

The phase transition of multiferroic $BiFeO_3$ was investigated through two very different experimental methods. PAC, which is an extremely sensitive method probing the sample on a local scale and XRD, which is a macroscopic method. The combination of both, combined with DFT simulations offers new possibilities in the characterisation of materials, like the characterisation of a phase transition in our work. The results of both experimental methods prove a phase transition from rhombohedral α-BFO in $R3c$ setting to orthorhombic β-BFO with its $Pbnm$ space group. Following the PAC results, two clearly distinguishable probe environments, also separated through their appearance on the temperature range, are detected. One, the lower frequency, symmetric fraction is indicating the α-phase and the other, the higher frequency asymmetric fraction is indicating the β-phase as comparisons with the simulated values of the strength of the electric field gradient V_{zz} and its asymmetry parameter η show. The first order phase transition is forecast by the Cd probe ion as the preceding symmetry change of Bi-coordination is sensed. The phase transition point at 820°C is visible through a drop in quadrupole interaction frequency ω_0 which indicates the site symmetry change of the Bi position. On the other hand, following the XRD results, the phase transition happens at a transition temperature at 818°C as this is the only temperature point where both phases appear simultaneously. Rietveld refinements of the recorded XRD patterns allow the visualisation of the characteristic volume contraction when the phase transition takes place as well as the phase fraction development over the temperature range. XRD sweep measurements covering characteristic peak change behaviour indicating the phase change, resulted in a transition temperature of 820°C when the temperature was increased and a transition temperature of 816°C - 812°C when the temperature was decreased, thus indicating a small hysteresis effect of about 4-8K. The appearance of the ternary phases $Bi_2Fe_4O_9$ and $Bi_{25}FeO_{39}$ was observed in the XRD measurements and shortly investigated. The results agree with most findings of already existing literature. Phase fractions of the ternary phases were not visible in the PAC results. Problems with the chemical stability of BFO at elevated temperatures point out the importance of well adjusted XRD measurement programs in order to keep measurement times as short as possible. Also the choice of the right material of the sample holder, especially when only having a limited amount of samples available, appeared to be an important factor for a successive measurement.

Future research on the α-β phase transition of multiferroic bismuth ferrite could include PAC measurements using different probe ions, which possibly find other equilibrium positions within the crystal. This could be interesting to investigate the phase transition from another point of view, or better said, from the view of another atom position within the crystal lattice. Supported by XRD measurements, I am certain that, also with different probes, the phase transition can be investigated in a similar precision.

Bibliography

[1] Ekhard KH Salje. Ferroelastic materials. *Annual Review of Materials Research*, 42:265–283, 2012.

[2] Joseph Valasek. Piezo-electric and allied phenomena in rochelle salt. *Physical review*, 17(4):475, 1921.

[3] Konrad Kopitzki and Peter Herzog. *Einführung in die Festkörperphysik*, volume 7. Springer, 2017.

[4] Sang-Wook Cheong and Maxim Mostovoy. Multiferroics: a magnetic twist for ferroelectricity. *Nature materials*, 6(1):13, 2007.

[5] Mois Ilia Aroyo. *International Tables for Crystallography*. Wiley Online Library, 2013.

[6] Kenji Uchino. *Ferroelectric devices*. CRC press, 2018.

[7] M. Reissner S. Bühler-Paschen, H. Michor. Skript Festkörperphysik I, 2018.

[8] Ekhard KH Salje. Ferroelasticity. *Contemporary Physics*, 41(2):79–91, 2000.

[9] Nicola A Hill. Why are there so few magnetic ferroelectrics?, 2000.

[10] Nicola A Spaldin and Manfred Fiebig. The renaissance of magnetoelectric multiferroics. *Science*, 309(5733):391–392, 2005.

[11] Manfred Fiebig. Revival of the magnetoelectric effect. *Journal of Physics D: Applied Physics*, 38(8):R123, 2005.

[12] Liliana Mitoseriu. Magnetoelectric phenomena in single-phase and composite systems. *Boletin de la Sociedad Espanola de Ceramica y Vidrio*, 44(3):177–184, 2005.

[13] H Béa, M Gajek, M Bibes, and A Barthélémy. Spintronics with multiferroics. *Journal of Physics: Condensed Matter*, 20(43):434221, 2008.

[14] Yaojin Wang, Xiangyong Zhao, Wenning Di, Haosu Luo, and Siu Wing Or. Magnetoelectric voltage gain effect in a long-type magnetostrictive/piezoelectric heterostructure. *Applied physics letters*, 95(14):143503, 2009.

[15] MI Bichurin, VM Petrov, RV Petrov, GN Kapralov, Yu V Kiliba, FI Bukashev, A Yu Smirnov, and AS Tatarenko. Magnetoelectric microwave devices. *Ferroelectrics*, 280(1):211–218, 2002.

[16] Manuel Bibes and Agnès Barthélémy. Multiferroics: Towards a magnetoelectric memory. *Nature materials*, 7(6):425, 2008.

[17] Ulrich Müller. *Anorganische Strukturchemie.* Springer, 2006.

[18] AM Glazer. The classification of tilted octahedra in perovskites. *Acta Crystallographica Section B: Structural Crystallography and Crystal Chemistry*, 28(11):3384–3392, 1972.

[19] Oliver Bock and Ulrich Müller. Symmetrieverwandtschaften bei varianten des perowskit-typs. *Acta Crystallographica Section B: Structural Science*, 58(4):594–606, 2002.

[20] Matjaz Valant, Anna-Karin Axelsson, and Neil Alford. Peculiarities of a solid-state synthesis of multiferroic polycrystalline bifeo3. *Chemistry of Materials*, 19(22):5431–5436, 2007.

[21] R. Haumont, J. Kreisel, P. Bouvier, and F. Hippert. Phonon anomalies and the ferroelectric phase transition in multiferroic bifeo$_3$. *Phys. Rev. B*, 73:132101, Apr 2006.

[22] Ratnakar Palai, Ram Katiyar, Hans Schmid, P. Tissot, S. Clark, Jv Robertson, Simon Redfern, G. Catalan, and J. Scott. Beta phase and gamma-beta metal-insulator transition in multiferroic bifeo3. *Phys. Rev. B*, 77, 01 2008.

[23] R Haumont, Igor A Kornev, S Lisenkov, L Bellaiche, J Kreisel, and B Dkhil. Phase stability and structural temperature dependence in powdered multiferroic bifeo 3. *Physical review B*, 78(13):134108, 2008.

[24] Igor A. Kornev, S. Lisenkov, R. Haumont, B. Dkhil, and L. Bellaiche. Finite-temperature properties of multiferroic bifeo$_3$. *Phys. Rev. Lett.*, 99:227602, Nov 2007.

[25] Donna C. Arnold, Kevin S. Knight, Finlay D. Morrison, and Philip Lightfoot. Ferroelectric-paraelectric transition in bifeo$_3$: Crystal structure of the orthorhombic β phase. *Phys. Rev. Lett.*, 102:027602, Jan 2009.

[26] Sverre M Selbach, Thomas Tybell, Mari-Ann Einarsrud, and Tor Grande. The ferroic phase transitions of bifeo3. *Advanced materials*, 20(19):3692–3696, 2008.

[27] Jie Wei, Chunfang Wu, Tiantian Yang, Zhibin Lv, Zhuo Xu, Dawei Wang, Raphael Haumont, and Zhenxiang Cheng. Temperature-driven multiferroic phase transitions and structural instability evolution in lanthanum-substituted bismuth ferrite. *The Journal of Physical Chemistry C*, 123(7):4457–4468, 2019.

[28] Gustau Catalan and James F. Scott. Physics and applications of bismuth ferrite. *Advanced Materials*, 21(24):2463–2485, 2009.

[29] Koichi Momma and Fujio Izumi. Vesta 3 for three-dimensional visualization of crystal, volumetric and morphology data. *Journal of applied crystallography*, 44(6):1272–1276, 2011.

[30] Antonio Perejon, Pedro E Sanchez-Jimenez, Jose M Criado, and Luis A Perez-Maqueda. Thermal stability of multiferroic bifeo3: kinetic nature of the β–γ transition and peritectic decomposition. *The Journal of Physical Chemistry C*, 118(45):26387–26395, 2014.

[31] F. Kubel and H. Schmid. Structure of a ferroelectric and ferroelastic monodomain crystal of the perovskite bifeo3. *Acta Crystallographica Section B*, 46(6):698–702.

[32] Delphine Lebeugle, Dorothée Colson, A Forget, Michel Viret, AM Bataille, and A Gukasov. Electric-field-induced spin flop in bifeo 3 single crystals at room temperature. *Physical review letters*, 100(22):227602, 2008.

[33] LW Martin, SP Crane, YH Chu, MB Holcomb, M Gajek, Mark Huijben, Chan-Ho Yang, N Balke, and R Ramesh. Multiferroics and magnetoelectrics: thin films and nanostructures. *Journal of Physics: Condensed Matter*, 20(43):434220, 2008.

[34] Claude Ederer and Nicola A Spaldin. Weak ferromagnetism and magnetoelectric coupling in bismuth ferrite. *Physical Review B*, 71(6):060401, 2005.

[35] Rakesh Dogra, A.P. Byrne, and Mark C. Ridgway. The potential of the perturbed angular correlation technique in characterizing semiconductors. *Journal of electronic materials*, 38(5):623–634, 2009.

[36] H. Frauenfelder and R.M. Steffen. Alpha-, beta-, and gamma-ray spectroscopy. *vol*, 2, 1965.

[37] Peter Friedsam. *Anorganische nichtmetallische Festkörper ohne Translationssymmetrie untersucht mit der Methode der gestörten γ-γ-Winkelkorrelation.* PhD thesis, Dissertation, Universität Bonn, 2000.

[38] J. G. Correia. Private communications. September 2018.

[39] J. Horta D. Silva. Interlude, https://www.uni-leipzig.de/.

[40] Muhammed Türker. Analyse zur bildung atomarer defektkomplexe nach dotierung von cadmium-tellurid und zink-oxid. 2012.

[41] J .G. Correia for GFIT19 and N. P. Barradas for NNFIT programs (PAC MANual Lisbon 1992).

[42] R Catherall, W Andreazza, M Breitenfeldt, A Dorsival, GJ Focker, TP Gharsa, TJ Giles, JL Grenard, F Locci, P Martins, et al. The isolde facility. *Journal of Physics G: Nuclear and Particle Physics*, 44(9):094002, 2017.

[43] Karl Johnston, Juliana Schell, JG Correia, M Deicher, HP Gunnlaugsson, AS Fenta, E David-Bosne, ARG Costa, and Doru C Lupascu. The solid state physics programme at isolde: recent developments and perspectives. *Journal of Physics G: Nuclear and Particle Physics*, 44(10):104001, 2017.

[44] Juliana Schell, Peter Schaaf, and Doru C Lupascu. Perturbed angular correlations at isolde: A 40 years young technique. *AIP Advances*, 7(10):105017, 2017.

[45] Marc De Graef and Michael E McHenry. *Structure of materials: an introduction to crystallography, diffraction and symmetry.* Cambridge University Press, 2012.

[46] Lothar Spieß, Herfried Behnken, Christoph Genzel, Robert Schwarzer, and Gerd Teichert. *Moderne Röntgenbeugung*, volume 2. Springer, 2009.

[47] Universität Duisburg Essen, Institut für Materialwissenschaft. `https://www.uni-due.de/materials/index_eng.shtml`.

[48] MA Nagl, MB Barbosa, U Vetter, JG Correia, and HC Hofsäss. A new tool for the search of nuclides with properties suitable for nuclear solid state physics based on the evaluated nuclear structure data files. *Nuclear Instruments and Methods in Physics Research Section A: Accelerators, Spectrometers, Detectors and Associated Equipment*, 726:17–30, 2013.

[49] Jean Blachot. Nuclear data sheets for a = 111. *Nuclear Data Sheets*, 110(6):1239 – 1407, 2009.

[50] Juliana Schell, Doru C Lupascu, João Guilherme Martins Correia, Artur Wilson Carbonari, Manfred Deicher, Marcelo Baptista Barbosa, Ronaldo Domingues Mansano, Karl Johnston, Ibere S Ribeiro, Isolde Collaboration, et al. In and cd as defect traps in titanium dioxide. *Hyperfine Interactions*, 238(1):2, 2017.

[51] J.F. Ziegler. Srim-2013 software package, http://www.srim.org.

[52] Markus Jäger, Kornelius Iwig, and Tilman Butz. A compact digital time differential perturbed angular correlation-spectrometer using field programmable gate arrays and various timestamp algorithms. *Review of Scientific Instruments*, 82(6):065105, 2011.

[53] G Kresse et al. G. kresse and j. furthmüller, phys. rev. b 54, 11169 (1996). *Phys. Rev. B*, 54:11169, 1996.

[54] J. N. Gonçalves. Private communications. September 2018.

[55] Heinz Haas, Stephan PA Sauer, L Hemmingsen, Vladimir Kell, and Pengwei W Zhao. Quadrupole moments of cd and zn nuclei: When solid-state, molecular, atomic, and nuclear theory meet. *EPL (Europhysics Letters)*, 117(6):62001, 2017.

[56] Julian Gebhardt and Andrew M Rappe. Doping of bifeo 3: A comprehensive study on substitutional doping. *Physical Review B*, 98(12):125202, 2018.

[57] Jean-Michel Moreau, Christian Michel, Robert Gerson, and William Joseph James. Ferroelectric bifeo3 x-ray and neutron diffraction study. *Journal of Physics and Chemistry of Solids*, 32(6):1315–1320, 1971.

[58] NP Barradas, Michel Rots, AA Melo, and JC Soares. Magnetic anisotropy and temperature dependence of the hyperfine fields of cd 111 in single-crystalline cobalt. *Phys. Rev. B*, 47(14):8763, 1993.

[59] M Forker. The problematic of the derivation of the electric fieldgradient asymmetry parameter from tdpac measurements or mössbauer spectroscopy in imperfect crystal lattices. *Nuclear Instruments and Methods*, 106(1):121–126, 1973.

[60] RD T Shannon and C Tfc Prewitt. Effective ionic radii in oxides and fluorides. *Acta Crystallogr. Sect. B*, 25(5):925–946, 1969.

[61] Malcolm E Lines and Alastair M Glass. *Principles and applications of ferroelectrics and related materials*. Oxford university press, 2001.

[62] GNP Oliveira, RC Teixeira, RP Moreira, JG Correia, JP Araújo, and AML Lopes. Local inhomogeneous state in multiferroic smcro 3. *Sci. Rep.*, 10(1):1–12, 2020.

[63] Todd M Rearick, Gary L Catchen, and James M Adams. Combined magnetic-dipole and electric-quadrupole hyperfine interactions in rare-earth orthoferrite ceramics. *Phys. Rev. B*, 48(1):224, 1993.

[64] MB Bellakki and V Manivannan. Synthesis, and study of magnetic properties, of bi 1- x cd x feo 3. *J. Mater. Sci.*, 45(4):1137–1142, 2010.

[65] B Ishaq, G Murtaza, S Sharif, M Azhar Khan, Naeem Akhtar, IG Will, Murtaza Saleem, and Shahid M Ramay. Investigating the effect of cd-mn co-doped nano-sized bifeo3 on its physical properties. *Results Phys.*, 6:675–682, 2016.

[66] W Sato, S Komatsuda, H Shimizu, R Moriichi, S Abe, S Watanabe, S Komatsu, T Terai, S Kawata, and Y Ohkubo. Dynamic motion and freezing of polaronic local structures in a colossal-magnetoresistive perovskite manganite la 0.7 ca 0.3 mno 3 detected with radioactive nuclei. *Phys. Rev. B*, 100(18):184111, 2019.

[67] Antonio Perejon, Pedro E Sanchez-Jimenez, Jose M Criado, and Luis A Perez-Maqueda. Thermal stability of multiferroic bifeo3: kinetic nature of the β–γ transition and peritectic decomposition. *The Journal of Physical Chemistry C*, 118(45):26387–26395, 2014.

[68] Sverre M Selbach, Mari-Ann Einarsrud, and Tor Grande. On the thermodynamic stability of bifeo3. *Chemistry of Materials*, 21(1):169–173, 2008.

[69] TT Carvalho and PB Tavares. Synthesis and thermodynamic stability of multiferroic bifeo3. *Materials Letters*, 62(24):3984–3986, 2008.

[70] Matjaz Valant, Anna-Karin Axelsson, and Neil Alford. Peculiarities of a solid-state synthesis of multiferroic polycrystalline bifeo3. *Chemistry of Materials*, 19(22):5431–5436, 2007.

[71] C Ternon, J Thery, T Baron, C Ducros, F Sanchette, and J Kreisel. Structural properties of films grown by magnetron sputtering of a bifeo3 target. *Thin Solid Films*, 515(2):481–484, 2006.

List of Figures